*nanomaterials*

MDPI

*Article*

# Segmental Mobility, Interfacial Polymer, Crystallization and Conductivity Study in Polylactides Filled with Hybrid Lignin-CNT Particles

**Panagiotis A. Klonos [1,2,*], Rafail O. Ioannidis [2], Andreas Pitsavas [2], Nikolaos D. Bikiaris [2], Sofia P. Makri [3], Stefania Koutsourea [3], Alexios Grigoropoulos [3], Ioanna Deligkiozi [4], Alexandros Zoikis-Karathanasis [3], Apostolos Kyritsis [1] and Dimitrios N. Bikiaris [2]**

[1] Dielectrics Research Group, Department of Physics, National Technical University of Athens, Zografou Campus, GR-15780 Athens, Greece; akyrits@central.ntua.gr
[2] Laboratory of Polymer Chemistry and Technology, Department of Chemistry, Aristotle University of Thessaloniki, GR-54124 Thessaloniki, Greece; rafailio@chem.auth.gr (R.O.I.); apitsava@chem.auth.gr (A.P.); nikompik@pharm.auth.gr (N.D.B.); dbic@chem.auth.gr (D.N.B.)
[3] Creative Nano PC, 43 Tatoiou, Metamorfosi, GR-14451 Athens, Greece; s.makri@creativenano.gr (S.P.M.); s.koutsourea@creativenano.gr (S.K.); a.grigoropoulos@creativenano.gr (A.G.); a.karathanasis@creativenano.gr (A.Z.-K.)
[4] AXIA Innovation GmbH, Fritz-Hommel-Weg 4, 80805 München, Germany; ide@axia-innovation.com
* Correspondence: pklonos@central.ntua.gr

**Abstract:** A newly developed series of polylactide (PLA)-based composites filled with hybrid lignin–carbon nanotube (CNTs) particles were studied using thermal and dielectric techniques. The low CNT content (up to 3 wt%) aimed to create conductive networks while enhancing particle–polymer adhesion. For comparison, PLA composites based on lignin and CNTs were also examined. Although infrared spectroscopy showed no significant interactions, calorimetry and dielectric spectroscopy revealed a rigid interfacial PLA layer exhibiting restricted mobility. The interfacial polymer amount was found to increase monotonically with the particle content. The hybrid-filled PLA composites exhibited electrical conductivity, whereas PLA/Lignin and PLA/CNTs remained insulators. The result was indicative of a synergistic effect between lignin and CNTs, leading to lowering of the percolation threshold to 3 wt%, being almost ideal for sustainable conductive printing inks. Despite the addition of lignin and CNTs at different loadings, the glass transition temperature of PLA (60 °C) decreased slightly (softer composites) by 1–2 K in the composites, while the melting temperature remained stable at ~175 °C, favoring efficient processing. Regarding crystallization, which is typically slow in PLA, the hybrid lignin/CNT particles promoted crystal nucleation without increasing the total crystallizable fraction. Overall, these findings highlight the potential of eco-friendly conductive PLA composites for new-generation applications, such as printed electronics.

**Keywords:** polylactide; hybrid lignin–CNT; segmental mobility; electrical conductivity; rigid amorphous fraction



Academic Editor: Antonios Kelarakis

Received: 24 March 2025
Revised: 18 April 2025
Accepted: 24 April 2025
Published: 26 April 2025

**Citation:** Klonos, P.A.; Ioannidis, R.O.; Pitsavas, A.; Bikiaris, N.D.; Makri, S.P.; Koutsourea, S.; Grigoropoulos, A.; Deligkiozi, I.; Zoikis-Karathanasis, A.; Kyritsis, A.; et al. Segmental Mobility, Interfacial Polymer, Crystallization and Conductivity Study in Polylactides Filled with Hybrid Lignin-CNT Particles. *Nanomaterials* **2025**, *15*, 660. https://doi.org/10.3390/nano15090660



## 1. Introduction

Poly (lactic acid), or else, polylactide (PLA), is a vastly studied aliphatic polyester that has found use in various applications, from the everyday life to academia and industry [1–3]. PLA, like many other known polymers, combines a superior performance, effectiveness and economic processing [4,5] with sustainability, serving as a 'green polymer' [6,7]. The green character of PLA owes to the potential for its synthesis from renewable

resources, such as corn starch, beet or sugar cane and potatoes [8,9], in addition to being relatively non-toxic or else biocompatible [10]. Thus, PLA has been exploited as a key polymer in many applications, for example, in packaging [10–12], in 3D-printing devices [13–15] and in bioengineering and biomedicine [16–18].

PLA demonstrates high thermal and chemical stability [19] and, simultaneously, relatively low glass transition temperatures, $T_g$~50–60 °C, and melting temperatures, $T_m$~160–190 °C [1,20–23]. The latter facts set the processing of this polymer as relatively effective, mild and economically beneficial, always, compared to other known industrial polymers synthesized employing fossil-based resources (polyethylene, polystyrene, poly$\alpha$crylates, etc.). The second major beneficial property of PLA is its compatibility with many other polymers, both green and not. There are numerous studies in the literature that prove the successful combination of PLA with other polymers in the form of copolymers, interpenetrating polymer networks and polymeric mixtures [3,23,24]. Next to these aspects, the semicrystalline character of PLA is of major importance. The degree of crystallinity and the semicrystalline morphology (size, distribution and interconnectivity of the crystals) of this polyester can be quite easily tuned to a wide extent. The tuning can be achieved either by the ab initio structure of PLA, namely, the low-high molar mass and the L/D -lactide stereoisomeric ratio, as well as by thermal processing [22,25,26] and the use of additives (e.g., nano-inclusions) [27,28]. The aspects of crystallinity are of severe importance, as they are tightly connected to both the macro- and nano-scopic performance of the materials, e.g., mechanical [27,29], the $T_g$ [21,22], small molecules permeation [30,31], heat transport [32,33] and even compostability [34,35]. An additional crucial aspect regarding polymers and polymer nanocomposites is the electrical conductivity. While most of the known polymers are insulators, due to the absence of free charges (electrons), the dispersion of conducting particles to the polymer matrix may lead to the formation of continuous conducting paths throughout the nanocomposite matrix (percolation theory) [36]. Such particles can be, for example, the carbon nanotubes, graphene platelets or metallic nanoparticles (Ag, Cu, etc) [37,38]. This is actually one of the goals of the present study, i.e., the application of polymer nanocomposites within printing inks applications. Among others, the manipulation of the conductivity of the nanocomposite provides additional potential for applications, for example, in health monitoring and sensors [39–42].

Regarding polymer composites and nanocomposites, the most widely employed reinforcing means are inorganic particles of various geometries, namely, spherical particles (e.g., silica), nano-sheets and nano-clays (e.g., graphene and montmorillonite) and nanotubes (e.g., carbon nanotubes). In the modern economic frame of green and circular economy, we witness a shift toward the development of completely green and renewable composites [43–46]. Lignin is one among the most promising candidates for replacing the conventional fillers. Lignin is usually addressed as soda- or kraft-lignin [47]. It is an aromatic biopolymer of, however, relatively high $T_g$ ($T_g$ > 100 °C) [48], which can be isolated from bio-resources, in particular, lignocellulosic biomass. After cellulose, lignin is considered to be the second most abundant natural polymer [49,50], demonstrating the combination of low toxicity with high biocompatibility. It exhibits a variation of functional groups and occupies high carbon amounts, with the latter being potentially transformed into composites and carbon-rich materials [47]. The addition of lignin in PLA (and other polyesters) has been proven to be a good means to enhance the antioxidation and antibacterial performance [51–54]. Despite the extensive amount of literature on neat PLA and PLA filled with conventional nano- and micro- particles, less attention has been paid to biobased polymer composites. Furthermore, there is still much space for studies focusing on lignin-filled PLA composites [54–57].

In the present work, we have prepared a series of PLA-based composites, within which lignin was the main reinforcing means, via simple methods (solutions' casting and mixing). In particular, we added hybrid particles containing 90 wt% soda lignin and 10 wt% multi-walled carbon nanotubes (MWCNTs and CNTs, for the sake of simplicity). The amount of hybrid lignin–CNT particles varied between 0.5 and 30 wt%. Following the exact preparation method, we also prepared a short series of PLA/Lignin and PLA/CNT composites, to be studied comparatively with the PLA/hybrid. Among the structure–properties relationships being investigated here, by known methods for examining structure, interactions, thermal transitions and molecular mobility, we studied the electrical conductivity of the systems. Among others, we aimed to investigate whether an interfacial polymer layer in the composites is formed in addition to the formation of electronic conducting paths (via CNTs) throughout the PLA matrix. This is because these 'green composites' are envisaged as conductive fillers in inks, within which the existence and potential manipulation of electrical conductivity is wanted in order to manufacture printed electronics. To directly assess the impact of the hybrid particles with those of neat lignin and neat CNTs, the conductivity results were also compared with those of neat CNTs at similar amounts. Since PLA is semicrystalline, in order to assess the direct effects of the fillers on the various properties (i.e., glass transition, segmental dynamics, electrical conductivity), the main study involved the materials in the amorphous state, whereas the crystallinity aspects are studied secondly.

## 2. Materials and Methods

### *2.1. Materials*

The materials of the main investigation are composites based on PLA filled with 0.5–30 wt% lignin–CNT hybrid particles. The hybrid materials consist of soda lignin/CNT with a 90/10 ratio (wt/wt), synthesized by Creative Nano PC (Athens, Greece). Hybrids were synthesized via a patented ultrasound-assisted method [58]. Soda lignin (Protobind 1000) was purchased from Tanovis AG (Rüschlikon, Switzerland) and MWCNTs with >96% purity and outside diameter 8–18 nm were purchased from Nanografi (Ankara, Turkey), whereas the Luminy® PLA L175 of melt flow index (MFI) at 8 g/10 min (Flow, 210 °C/2.16 kg) and 3 g/10 min (Flow, 190 °C/2.16 kg) was purchased from Corbion N.V. (Gorinchem, The Netherlands).

Briefly, masterbatches of PLA/hybrid were prepared by solution casting, in particular, of PLA/chloroform at 10% $w/v$ and, subsequently, melt-mixing. First, the hybrid additives at wanted mass amounts were diluted in chloroform at 3% $w/v$ and subjected to ultrasonication. The said solutions were mixed and mechanically stirred. The composites were allowed to dry overnight, so that the excess chloroform was evaporated. Finally, the dried masterbatches and dried PLA were added to a melt-mixer, Haake–Buchler twin screw co-rotating extruder, and a mixing head with a volumetric capacity of 11 $cm^3$, operating at 190 °C and 30 rpm for 5 min. In total, seven PLA/Hybrid systems were prepared. For comparison of the hybrid particles' performance, we have also prepared and parallelly studied PLA-based systems filled with either neat lignin or neat CNTs at the loadings of 0.5, 1.0 and 2.5 wt%, via similar routes (i.e., three PLA/Lignin and three PLA/CNT samples).

The samples were mainly studied in the form of disks of ~1 mm in height (thickness) and ~20 mm in diameter, prepared by melt-pressing employing homemade molds.

### *2.2. Infrared Spectroscopy*

Attenuated total reflection Fourier transform infrared (ATR-FTIR) spectra were recorded on amorphous samples. The measurements were performed employing an IRTracer-100 spectrophotometer by Shimadzu (Kyoto, Japan) equipped with a QATR™

10 Single-Reflection ATR Accessory with a Diamond Crystal. The spectra were recorded in absorbance mode, within the wavenumber region from 400 to 4.000 $cm^{-1}$ at steps of 2 $cm^{-1}$. The presented spectra correspond to a total of 32 co-added scans, which were normalized and baseline corrected.

### *2.3. Scanning Electron Microscopy (SEM)*

To examine the micromorphology and filler distribution in the polymer matrix, we performed SEM measurements, by means of an emission scanning electron microscope (JEOL (Tokyo, Japan) JSM 7610F) operating at 5 kV. The SEM images were captured at the materials' cryo-fractured cross-sections, upon gold sputtering.

### *2.4. Differential Scanning Calorimetry (DSC)*

Conventional calorimetry was employed for the study of the polymeric thermal transitions within the temperature range from −10 to 200 °C in a high-purity nitrogen atmosphere. A TA Q200 DSC calorimeter (TA Instruments, New Castle, DE, USA) was employed for the thermal study, whereas the measurements were carried out on samples of ~7–9 mg in mass closed in aluminium standard TA pans. Prior to the measurements, the calorimeter had been properly calibrated for the temperature and enthalpy, using indium, and for the heat capacity, using sapphires.

A first heating scan from room temperature up to 200 °C was performed for all samples, in order to erase the thermal history and optimize the thermal contact between the sample and the pan. Then, two main scans were conducted, as follows. The first scan involved a fast cooling at non constant rates (i.e., 60–100 K/min), while the second scan involved a slower cooling at 20 K/min. The subsequent heating for both scans was carried out at the fixed heating rate of 10 K/min.

### *2.5. Broadband Dielectric Spectroscopy (BDS)*

The electrical conductivity at RT~20 °C was evaluated by dielectric spectroscopy [59] and by means of Novocontrol BDS setup (Novocontrol GmbH, Montabaur, Germany) on sample in the form of thin disks (~1 mm in thickness and 14–15 mm in diameter). Upon application of an alternate to the sample capacitor, the complex dielectric permittivity, $\varepsilon^* = \varepsilon' - i{\cdot}\varepsilon''$, was recorded in the frequency, $f$, range from $10^{-1}$ to $10^6$ Hz. The $f$ dependence of complex electrical conductivity, $\sigma^*$, was estimated from $\varepsilon^*$ via Equation (1):

$$\sigma^*(\omega) = i * \omega * \varepsilon_o * \varepsilon^*(\omega) \quad (1)$$

wherein $\omega$ is the angular frequency ($\omega = 2\pi{\cdot}f$) and $\varepsilon_0$ is the dielectric permittivity of the vacuum. The real part of $\sigma^*$ is taken as the AC conductivity, $\sigma'$.

Additionally, the segmental dynamics were studied by BDS by following the imaginary part of the dielectric permittivity, $\varepsilon''(f)$, at various temperatures from 30 up to 120 °C. $\varepsilon''(f)$ was isothermally recorded at steps of 5 and 10 K. We recall that the samples had been kept initially in the amorphous state by melting and fast cooling to room temperature (RT < $T_g$).

## 3. Results and Discussion

### *3.1. Structure—Dispersion of Particles*

Before presenting the results on the thermal transitions and molecular mobility, it is essential to provide a microscopic view of the studied samples. In Figure 1, we present selected SEM images for neat PLA and the PLA/lignin composites. Lignin seems to be very well dispersed throughout the PLA matrix, forming entities with sizes below 1 μm, in general. Obviously, larger lignin aggregates co-exist (up to 4–5 μm), especially for the composites with the larger loadings.

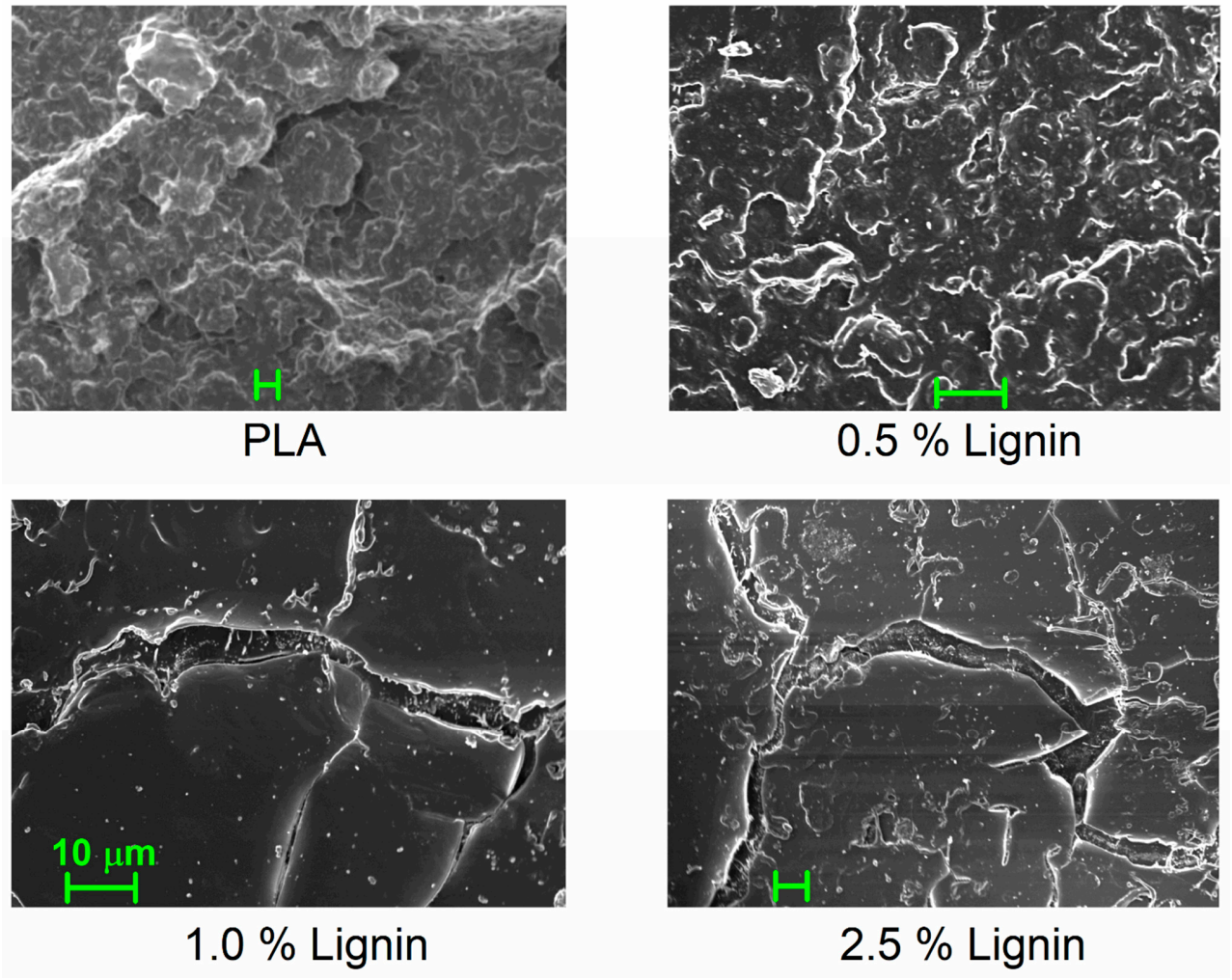


**Figure 1.** SEM images for neat PLA and PLA/lignin composites. The added scale bar corresponds to 10 μm for all images.

In Figure 2, we show SEM micrographs for the PLA/hybrid composites with loadings from 1 to 30% and at two magnifications (main and inset images). The hybrid particles dispersion is quite good throughout the polymer matrix. We would like to report that the shown images are actual representatives of the overall composite volume, not of a selection of the best recorded dispersions. The existence of the hybrid lignin–CNT entities can be seen within the images for loadings of 5–30%. The presence of CNTs is clear for all cases, whereas it is interesting that the dispersion of the CNTs themselves is quite good as well. Especially for the higher loadings of 10–30% hybrid, or else, 1–3% CNTs, some continuous CNT–CNT paths have been formed. This is expected to affect a series of macroscopic properties, in particular, the electrical conductivity, the latter being studied in a later section.

### *3.2. Glass Transition and Interfacial Adhesion*

Following are the results by calorimetry for scan 1. During the cooling scan at relatively fast rates, no exothermal event (peak) related to crystallization is recorded. Therefore, we consider the polymers amorphous at the beginning of the subsequent heating (Figure 3), at least up to temperatures closely above the glass transition. The main values of interest can be found in Table 1 and in the following figures. Within the temperature range studied and in the order of increasing temperature, single glass transition steps were recorded, as were cold crystallizations (2 peaks) and single melting events. Considering the numerous

published findings for PLA [21,25,60,61], we conclude that all the thermal events originate from PLA.

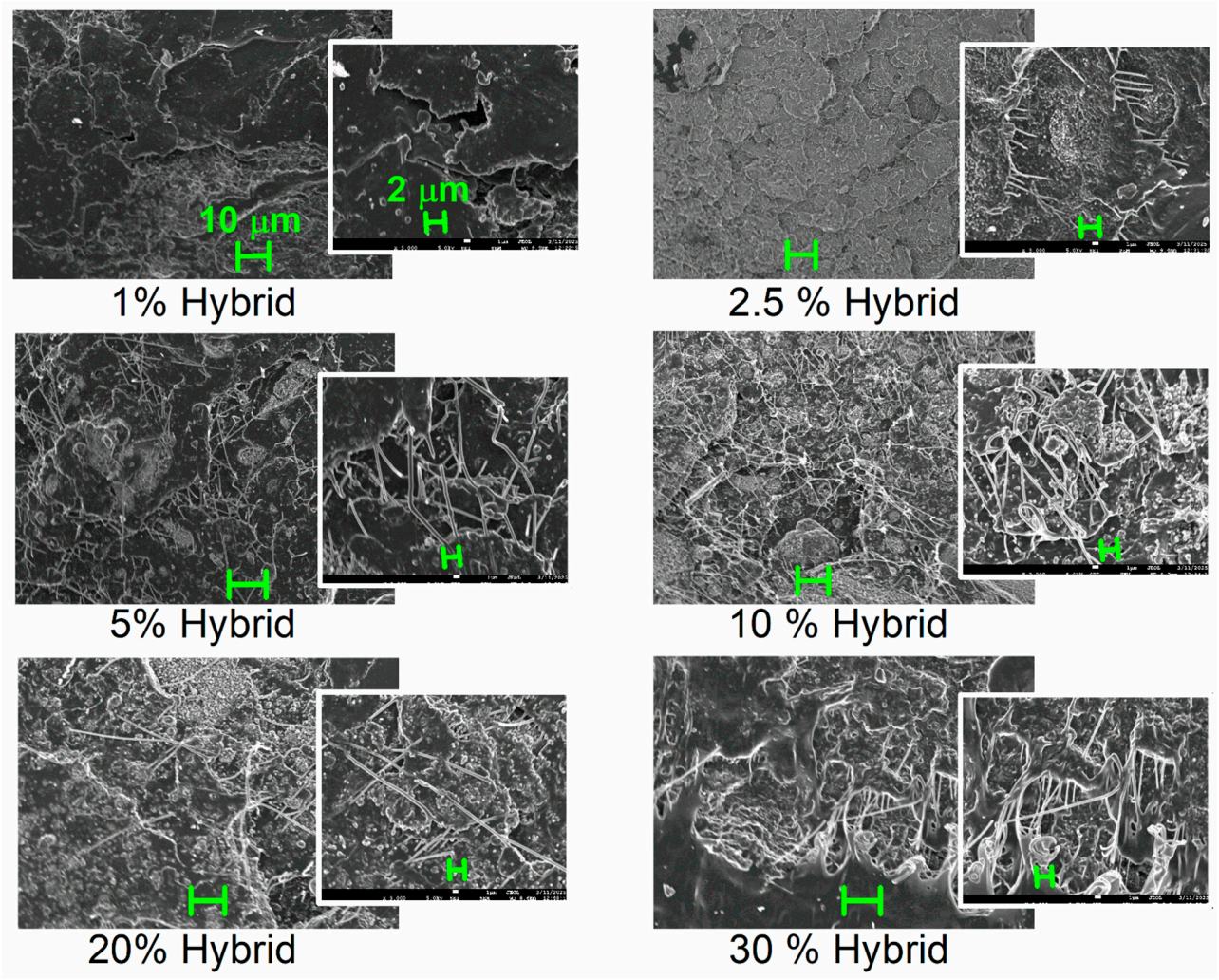


**Figure 2.** SEM images for all PLA/hybrid composites. The scale bars added to the main images correspond to 10 μm, whereas those added to the insets correspond to 2 μm.

Since we have preserved the amorphous character of PLA, we may seek for the direct effects of the hybrid particles on PLA. The glass transition offers this opportunity. In Figure 3b, we have focused on the glass transition, moreover, upon normalization of the thermograms to the mass of PLA and presenting the data in heat capacity, $c_p$, units. In addition, we vertically translated the heating traces, so that the low temperature-side baselines coincide for all samples. Regarding the temperature position of the glass transition step, a slight $T_g$ decrease is observed with the addition of particles, both hybrid and neat lignin. The characteristic $T_g$ values are presented in Figure 4a, showing a weak drop from 60 °C (neat PLA) by 2 K in the composites. Moderate effects on the $T_g$ have been presented in the past in PLA/CNT [62] and in PLA/CNT–lignin systems [63].

The most striking effect on glass transition is recorded on the strength of the transition, i.e., on the heat capacity change, $\Delta c_p$ (vertical arrow in Figure 3b). In the inset to Figure 4a, the $\Delta c_p$ of PLA (0.50 ± 0.1 J/g·K) exhibits a monotonic suppression with the filler addition. Since we have no other parameters implementing, e.g., a molecular weight change, the said suppression arises from the presence of the filler. In many previous works on polymer nanocomposites [61,64–67], the $\Delta c_p$ suppression has been connected to the presence of a formed interfacial polymer layer onto the fillers' surfaces. This layer is believed to extend

to a few nanometers—from the filler surface and to exhibit either an immobilization [64,65] or quite retarded mobility [66,68–70]. When being immobile, or else rigid, this polymer fraction obviously does not directly contribute to the glass transition. Therefore, a missing in $\Delta c_p$ is recorded. This rigid amorphous fraction, RAF, has been initially studied by Wunderlich [71], and a mathematical method for estimating its amount, based on $\Delta c_p$, has been proposed. That is expressed mathematically via Equation (2):

$$RAF = (1 - {}^{\Delta c_{p,norm}}/_{\Delta c_{p,matrix}}) \times 100\% \quad (2)$$

where in $\Delta c_{p,norm}$ corresponds to the composite and $\Delta c_{p,matrix}$ is the heat capacity change of the neat amorphous PLA.

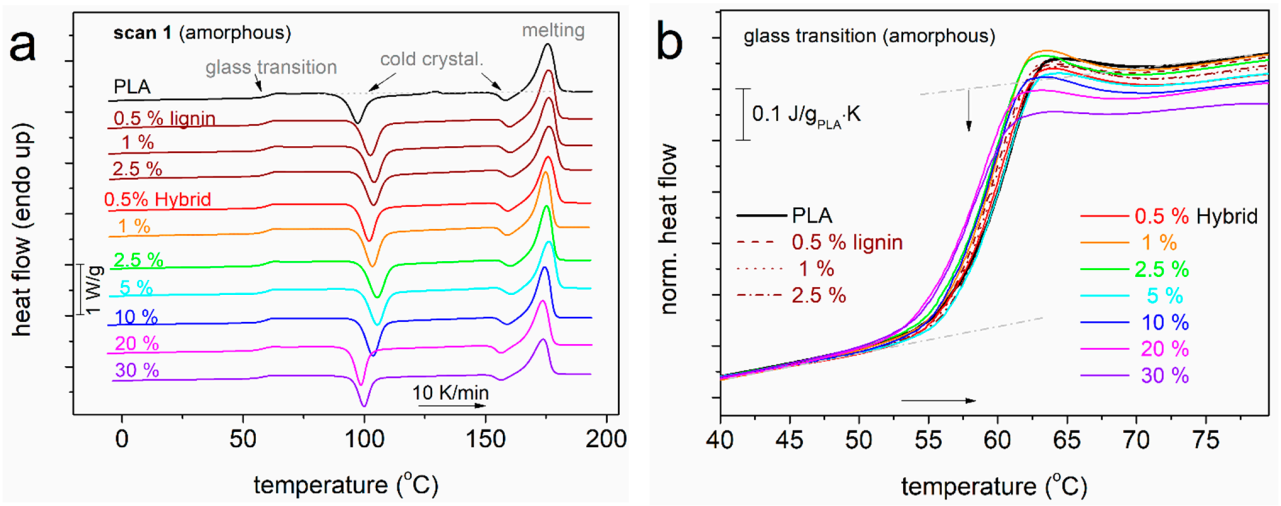


**Figure 3.** (**a**) Comparative DSC heating traces of scan 1. The shown heat flow is shown upon normalization to the sample mass (W/g). Indicated are the main thermal transitions recorded. (**b**) Details of the glass transition region, shown upon normalization of the recorded heat flow to the polymer mass and in $c_p$ units (J/$g_{PLA}$·K).

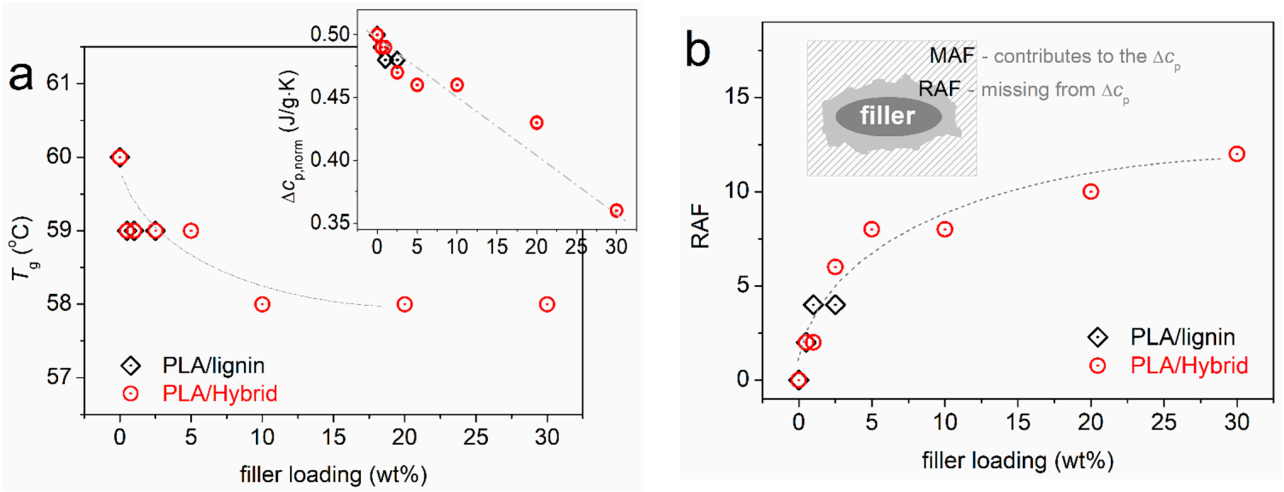


**Figure 4.** The filler content dependences of (**a**) glass transition temperature and heat capacity change (inset to (**a**)) and (**b**) the calculated rigid amorphous fraction (interfacial polymer) for all systems. Please note that the data refer to the polymers in the amorphous state. The added lines are simple eye guides. The inset to (**b**) presents a simplified schematic for rationalizing the existence of RAF in the polymer/filler composites.

**Table 1.** Samples under investigation and values of interest obtained by calorimetry: glass transition temperature, $T_g$, normalized heat capacity change, $\Delta c_{p,norm}$, calculated rigid amorphous fraction, RAF, in the amorphous state, low temperature cold crystallization temperature, $T_{cc1}$, melt crystallization temperature and normalized enthalpy, $T_c$ and $\Delta H_{c,norm}$, respectively, crystalline fraction estimated from the latter enthalpy, $CF_c$, and melting temperature, $T_m$.

| Sample | Lignin (wt%) | CNT (wt%) | DSC (Fast Cooled, Amorphous) | | | | DSC (Cooled at 20 K/min) | | | | |
|---|---|---|---|---|---|---|---|---|---|---|---|
| | | | $T_g$ (°C) | $\Delta c_{p,norm}$ ($J/g_{PLA} \cdot K$) | RAF (%) | $T_{cc1}$ (°C) | $T_c$ (°C) | $\Delta H_{c,norm}$ ($J/g_{PLA}$) | $CF_c$ (%) | $T_g$ (°C) | $T_m$ (°C) |
| PLA (neat) | 0 | 0 | 60 | 0.50 | 0 | 97 | 80 | 1.3 | 1 | 60 | 175 |
| PLA + 0.5% lignin | 0.5 | 0 | 59 | 0.49 | 2 | 102 | 92 | 2.3 | 2 | 59 | 176 |
| PLA + 1.0% lignin | 1.0 | 0 | 59 | 0.48 | 4 | 104 | 90 | 1.0 | 1 | 59 | 176 |
| PLA + 2.5% lignin | 2.5 | 0 | 59 | 0.48 | 4 | 104 | 89 | 1.8 | 2 | 59 | 176 |
| PLA + 0.5% hybrid | 0.45 | 0.05 | 59 | 0.49 | 2 | 102 | 92 | 1.5 | 2 | 59 | 176 |
| PLA + 1.0% hybrid | 0.9 | 0.1 | 59 | 0.49 | 2 | 103 | 91 | 1.3 | 1 | 59 | 175 |
| PLA + 2.5% hybrid | 2.25 | 0.25 | 59 | 0.47 | 6 | 105 | 92 | 1.8 | 2 | 58 | 175 |
| PLA + 5.0% hybrid | 4.5 | 0.5 | 59 | 0.46 | 8 | 105 | 89 | 1.4 | 2 | 59 | 175 |
| PLA + 10.0% hybrid | 9 | 1 | 58 | 0.46 | 8 | 104 | 92 | 2.0 | 2 | 61 | 174 |
| PLA + 20.0% hybrid | 18 | 2 | 58 | 0.45 | 10 | 99 | 97 | 26 | 28 | 57 | 174 |
| PLA + 30.0% hybrid | 27 | 3 | 58 | 0.44 | 12 | 100 | 94 | 14 | 15 | 57 | 174 |

The estimated RAF is listed in Table 1 and shown in Figure 4b. RAF increases monotonically with increasing the hybrid content from 2 to 12%; however, this is not linear [64,65,72]. The latter suggests that, most probably, the distribution of the hybrid particles is better for the lower contents and becomes worse for the higher ones [73], which is more or less the main situation for composites prepared by simple mixing [70]. However, we recall that from the SEM data (Figures 1 and 2), the dispersion of the fillers is quite good in all cases.

The formation of the interfacial rigid polymer layer is generally considered to be due to strong attractive interactions between the fillers and the neighboring polymer chains [69,73]. Regarding polyesters, such as PLA here, the interaction can be evidenced by a disturbance in the vibration of the ester bond (-C=O), located at their most polar site (carbonyl). The mentioned disturbance has been recorded, for example, by infra-red spectroscopy, as either an increasing contribution of the radiation absorbance at lower wavenumbers or as an overall migration of the absorbance peak toward lower wavenumbers.

Following previous methodologies, we present, in Figure 5, the FTIR spectra within the ester bond vibration band for PLA/lignin (Figure 5a) and PLA/hybrid (Figure 5b), with all systems being in the amorphous state. In none of the composites did we record such worth-noting disturbance of the ester bond peak. Therefore, we could conclude that the presence of RAF here could not be due to formed interfacial bonding, at least, not uniquely or to a vast extent, but to topological constraints imposed on the PLA chains. In this context, we recall that the composites preparation involved solution castings and mixings, thus implementing polymer chains with maximized degrees of motion freedom [74]. This could facilitate the entanglements between hybrid particles (CNTs) and the PLA chains to a high level [75]. Such entanglements can be also facilitated by the increase in the filler's specific surface area/surface roughness [66] and aspect ratio [28,33,76]. These are expected to increase with the involvement of CNTs, individually and in combination with lignin in the hybrids.

### *3.3. Effects on the Polymer Crystallization*

In this section, we discuss the effects imposed by the presence of lignin and hybrid particles on the crystallizability of PLA. In Figure 6, we present the DSC thermograms for scan 2, i.e., upon erasing the thermal history, cooling the samples at a moderate rate

(20 K/min, Figure 6a) and a subsequent heating (10 K/min, Figure 6b). During cooling, a weak exothermal peak is recorded in neat PLA at $T_c$ = 80 °C (Table 1), corresponding to the melt/hot crystallization. By recording the corresponding enthalpy change ($\Delta H_c$) and comparing it with the bibliographic value for the 100% crystalline PLA (~93 J/g) [77], we calculated the crystalline fraction as $CF_c$ = 1 wt%. The melt crystallization is very low also for the PLA/lignin and most PLA/hybrid systems. The exception to that is the case of 20% and 30% hybrid, within which the crystallization is strongly enhanced.

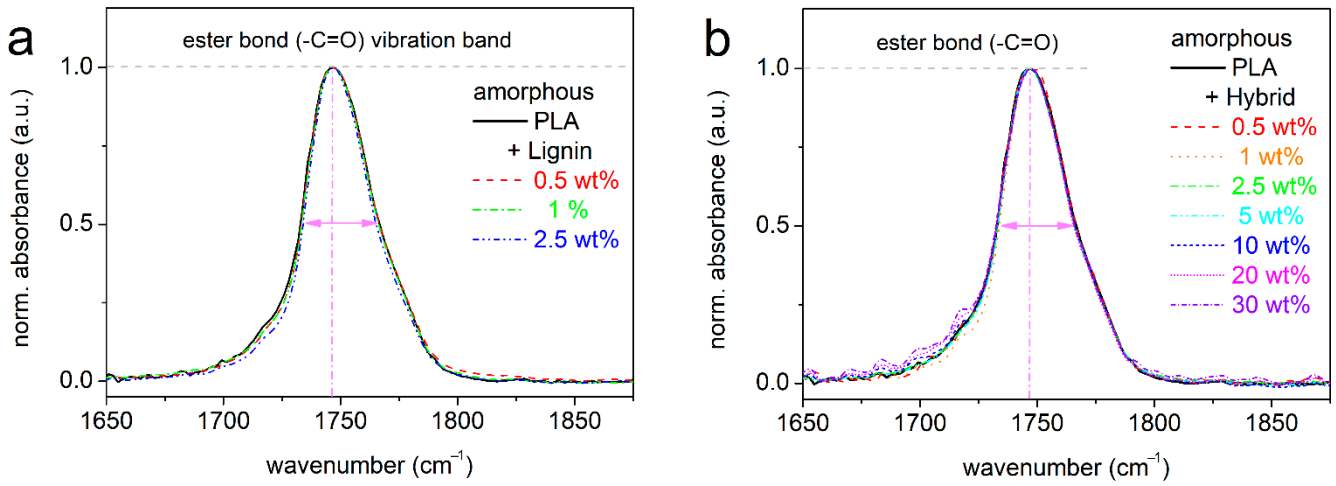


**Figure 5.** Comparative FTIR spectra focusing on the wavenumber band of absorbance arising from the vibration of the ester bond of PLA, shown for (**a**) PLA and PLA/lignin and (**b**) PLA and PLA/hybrid, all polymers being in the amorphous state. The absorbance peaks are shown upon shape normalization to the peak maxima.

The $T_c$ and $CF_c$ were also evaluated and are shown in Figure 7a and b, respectively, as a function of the filler loading. Independently from the filler type, $T_c$ increases significantly by 9–17 K in the composites. On first thought, this suggests that the fillers, in whole or in part, may act as crystallization nuclei. Then, $CF_c$ is, in general, low, 1–2%, which, combined with the elevated $T_c$, suggests an altered semicrystalline morphology. For example, we could expect that in the composites during melt crystallization, more crystals but ones of quite smaller sizes are formed. In the extreme cases of 20 and 30% hybrid, the high $T_c$ values are accompanied by a high $CF_c$ of ~28 and ~15%, respectively. We suspect that for these cases, the role of CNTs is quite strong in facilitating the crystallinity [28].

PLA is known to slowly and weakly crystallize, in general, compared with other semicrystalline polymers (polyethylene, polycaprolactone, etc.). This is evidenced, among other indicators, by the difficulty to crystallize during cooling and the evolution of crystallization also upon heating (cold crystallization, Figures 3a and 6b). The clearest view for cold crystallization is that shown in Figure 3a, as it involves the prior suppression of melt crystallization and the subjection of the sample to strong supercooling by fast cooling. The corresponding temperature of cold crystallization, $T_{cc}$, (Figure 7a) increases for low and moderate filler loadings and decreases for higher ones. In terms of the nucleation effects of lignin and hybrid, the results are compatible with those for the melt crystallization only for the high filler loadings. The evolution of cold crystallization is also connected with the mobility of the polymer chains, i.e., reflected on the $T_g$. In this context, the low-filled composites exhibit the highest $T_g$ (Figure 4a); thus, they exhibit slower diffusion of chains and, essentially, retarded development of cold crystallization, compared to the faster cold crystallization of the highly filled composites.

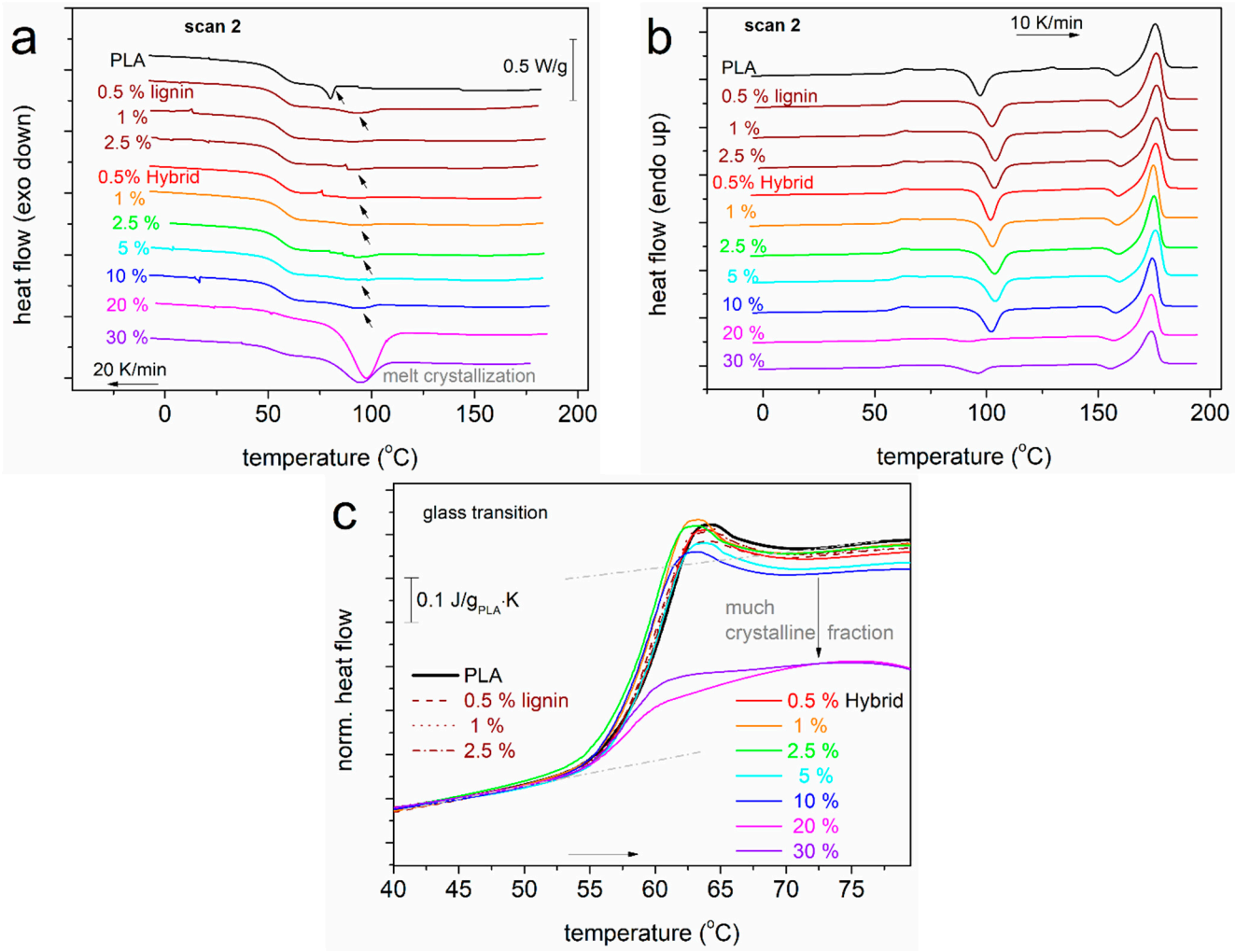


**Figure 6.** Comparative DSC traces for scan 2, namely, (**a**) during cooling from the melt state at 20 K/min and (**b**) during the subsequent heating at 10 K/min. The heat flows in (**a**,**b**) are shown upon normalization to the sample mass. (**c**) Details in the glass transition region for all samples, upon normalization of the heat flow to the polymer mass and in presented in $c_p$ units.

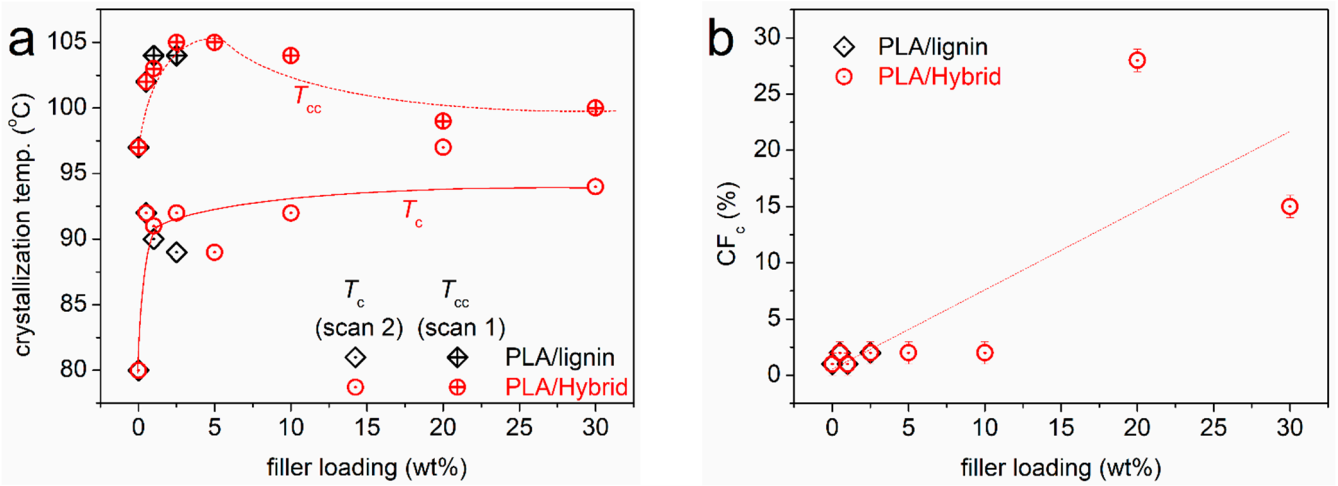


**Figure 7.** (**a**) The filler content dependences of $T_c$ and $T_{cc}$, from scans 2 and 1, respectively. The added lines are used as guides for the eyes. (**b**) The corresponding dependence of the calculated crystalline fraction during melt crystallization, $CF_c$. The added line corresponds to the linear fitting to all data.

The melting temperature, $T_m$ (Table 1), lying between 174 and 176 °C, demonstrates minor changes. Due to that, we expect insignificant changes in the quality of the formed crystals (size, density of the lamellae packing, etc.).

Finally, we should comment on the effects of crystallization on the glass transition. From Table 1 and in Figure 6c, we may conclude that the presence of the crystals is significant only when the $CF_c$ is worth noting. This happens for the cases of 10–30 wt% hybrid, where the effects are quite strong concerning the strength of the glass transition ($\Delta c_p$) rather than the $T_g$, which barely changes.

### *3.4. Electrical Conductivity Aspects*

BDS enables the evaluation of electrical conductivity, $\sigma_{AC}$, via the measurement of the dielectric permittivity function (Equation (1), [59]). As expected, the neat PLA and the PLA/lignin composites exhibit electrical insulating character. This is manifested in Figure 8, as the $\sigma_{AC}(f)$ in the recorded spectra at room temperature (RT < $T_g$) is, in general, low and $\sigma_{AC}$ is frequency dependent. In addition, the PLA/CNT systems are also electrical insulators, even at the higher CNT loading of 2.5%.

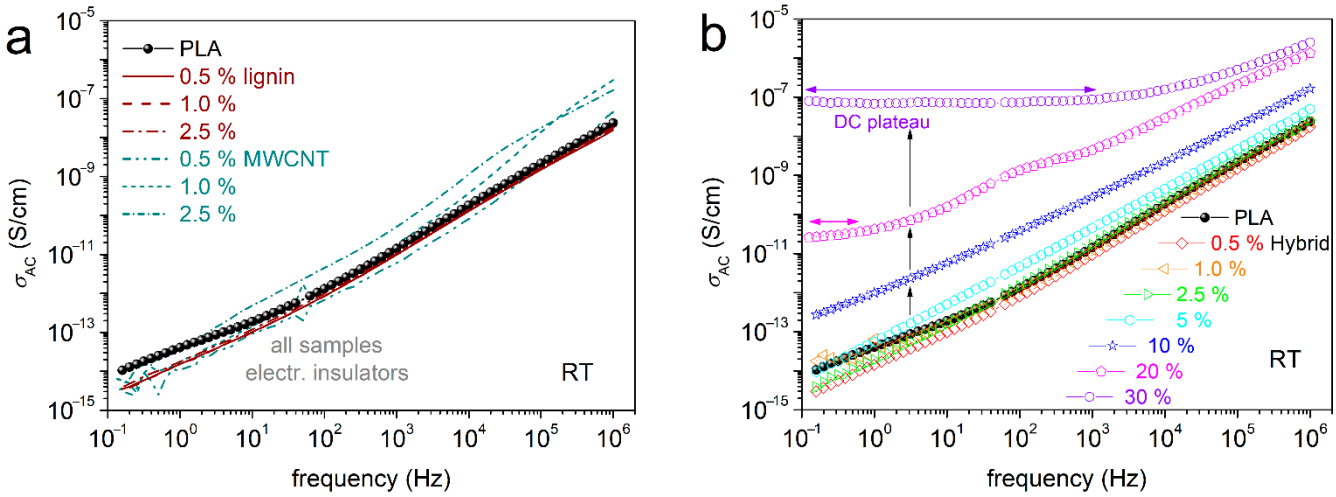


**Figure 8.** Comparative isothermal spectra of the real part of electrical conductivity (in AC), $\sigma_{AC}$, as a function frequency at RT~20 °C for (**a**) PLA, PLA/lignin and PLA/MWCNTs and (**b**) PLA and PLA/hybrid lignin–CNTs.

We recall that the composites have been prepared by simple methods, without the employment of any surface modifications for CNTs. In previous works on CNT-filled polymer nanocomposites (including PLA) involving simple mixing routes, the electrons percolation threshold, $p_c$ [36], has been found to be relatively high, e.g., between 5 and 6 wt%. This is in agreement with the discussed microscopic view for these composites (Figure 2). It is worth noting, on the other hand, that when more specific dispersion methodologies and CNT-surface modifications are involved, $p_c$ has been evaluated at quite low CNT fractions (0.06–0.7%) [37,78] or even extremely low ones (0.0025%) [38].

Coming back to our composites, the addition of hybrid in PLA induces the following impact on conductivity. In Figure 8b, for up to 5% hybrid, the composites preserve the insulating behavior. For 10% hybrid, an overall $\sigma_{AC}$ increase within the whole f range is recorded. Then, for gradually increasing the hybrid loading to 20 and 30%, $\sigma_{AC}$ exhibits a stronger rise, by orders of magnitude. Interestingly, the increase is accompanied by the formation of a plateau. The latter suggests the independence of σ from f, at least for the lower frequencies. Such a plateau in polymers, with absolute σ values from ~$10^{-8}$ to ~$10^{-6}$ S/cm, usually denotes the ions transport (ionic conductivity) throughout the rubbery

(liquid state) of the polymer matrix. This is not the case here, as PLA at RT is still in the glassy state and any ion transport is precluded. The plateau is recorded at both lower and higher temperatures. Therefore, we conclude that this plateau, else called the DC plateau, is due to the transport of electrons throughout the composites' volume. Obviously, this is the case for the formation of continuous (percolating) electrons paths via CNTs [36].

The results on the electrical conductivity can be summarized for all samples in Figure 9, wherein we have plotted the values for $\sigma_{AC}$ at the lowest f of recording, i.e., 100 mHz, against the filler loading, for PLA/lignin, PLA/hybrid and PLA/CNTs. In the main figure, we obtain an almost linear dependence of conductivity, with no exceptional behavior among the different filler types.

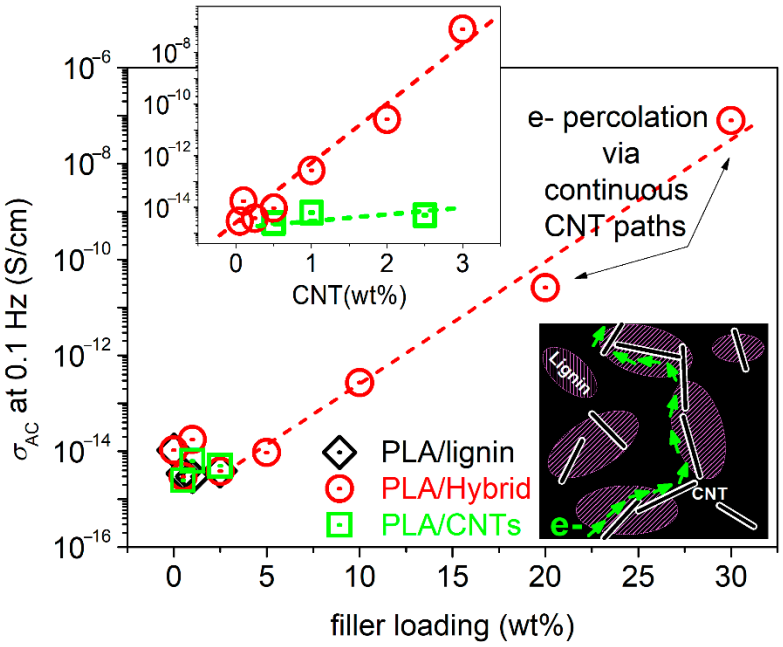


**Figure 9.** The filler wt% content dependence of the absolute conductivity, $\sigma_{AC}$, values at the lowest frequency of recording, for PLA/lignin, PLA/hybrid and PLA/CNT. The inset graph shows the respective dependence from $\sigma'$ directly from the CNT loading. The added scheme presents the estimated mechanism of electronic conductivity via percolating CNT paths.

Nevertheless, exploiting the knowledge that the unique free electron carriers here are the CNTs, in the inset to Figure 9, we plotted the CNT dependence of $\sigma_{AC}$. We observe a striking effect here. The same amount of CNTs imposes undetectable effects in conductivity when being mixed with PLA, whereas it introduces significant electron conduction when being introduced to PLA via the hybrid lignin–CNT entities. Most probably, this is an interesting case of a synergistic [79] CNT–lignin effect, in the sense of favoring the CNT–CNT percolation (schematic in Figure 9). The said effect should not be far from the reality, as recalling the SEM images of Figure 2, the CNTs were found to be concentrated within the lignin-rich areas. Within these domains, the possibility for CNT percolation is larger, as compared to the case of mixing PLA with neat CNTs. Obviously, this is a strong speculation and needs further experimental manifestation.

Apart from the interest from the physics point of view, the result of enhancing the electrical conductivity here for relatively low CNT loadings within a mostly green polymer composite is quite interesting and promising, envisaging certain applications (e.g., conducting printing inks, etc.).

We should mention, from the methodological point of view, that a 'precise' evaluation of $p_c$ for our systems from Figure 9 employing the percolation theory is precluded, due

to the relatively few points of the actually conductive composites. In addition to that, the almost linear trend of $\sigma_{DC}$ against the filler loading is not expected to produce a realistic/representative $p_c$ value.

### *3.5. Segmental Dynamics*

In the last section of this study, we investigate the segmental dynamics. This is achieved by following the formation of dielectric loss, $\varepsilon''$(f), peaks [80,81], which can be carried out only for the systems exhibiting an electronically insulating character. Therefore, PLA filled with 20 and 30% hybrid, which is electrically conductive, does not allow for such investigation. We also recall that for assessing the direct filler loading effects, the BDS measurements initiate with the polymers being in the amorphous state.

The segmental dynamics can be monitored by the dipolar relaxation of the dipole moments being perpendicular to the polymer chain backbone [59]. The dipoles exhibit 'recordable' relaxation times, $\tau_{rel}$, for temperatures around $T_g$ and higher. For such temperatures, the dielectric losses demonstrate the so-called $\alpha$ relaxation/process peak. The latter can be seen in Figure 10 (raw data) for selected systems and temperatures. With the temperature increasing gradually, the peaks migrate toward higher frequencies, as the polymer chains become more mobile. Thus, the dipolar $\tau_{rel}$ become gradually shorter. This is actually the reason for such a result to be referred to as 'dynamics' and the $\alpha$ relaxation being considered as the dielectric and dynamic analogue of the calorimetric glass transition. At temperatures above 85–90 °C, the amorphous polymer character gradually changes, as cold crystallization takes place. Please compare Figure 10a (BDS, blue arrow) with Figure 3a (DSC).

At the higher frequency side of Figure 10a and for temperatures below and close to $T_g$, a weak peak addressed as β is recorded. This peak is due to the relaxation of local groups in PLA (-C=O on the chain backbone, [80]), which is not studied here. Additional phenomena being recorded within the temperature range of the measurements are related to ionic conductivity and interfacial polarizations [59]. The ionic conductivity is recorded as a sharp linear-like increase in the $\varepsilon''$ at the lower frequency side of the spectra and for $T >> T_g$. Within similar frequency/temperature ranges, the interfacial polarization phenomena are recorded as strong peaks (not discussed further here).

Since the focus here is on the segmental relaxation, and in order to extract as much information as possible from the BDS data, we performed fitting [59] of $\varepsilon''$(f,T) by widely adopted mathematical model functions. The Havriliak–Negami (HN) function [59], described by Equation (3), was employed to fit the asymmetric peaks, in our case, the amorphous $\alpha$ relaxation.

$$\varepsilon^*(f) = \frac{\Delta\varepsilon}{\left[1 + \left(\frac{if}{f_0}\right)^{\alpha_{HN}}\right]^{\beta_{HN}}} + \varepsilon_\infty \quad (3)$$

In the HN function, $f_0$ is a characteristic frequency related to the frequency of maximum dielectric loss, $\varepsilon_\infty$ is a value of the real part of the dielectric permittivity ($\varepsilon'$) at $f >> f_0$, $\alpha_{HN}$ is a shape parameter that denotes the width of relaxations times range and $\beta_{HN}$ is another shape parameter that evaluates the symmetry of the $\varepsilon''$(f) peak. $\Delta\varepsilon$ is the dielectric strength (~magnitude of the peaks) or else the corresponding contribution of the dipoles to the dielectric permittivity. The same model can be fitted for symmetric peaks, if needed, and this is achieved by fixing the asymmetricity parameter $\beta_{HN}$ as 1. This way, the HN models becomes the so-called Cole–Cole function [59]. To fit the ionic conductivity contribution, a specific linear term is used, with a slope equal to ~1 [59].

The fitting process was 'critically' employed for all samples and two examples are demonstrated in Figure 11a for neat PLA and in Figure 11b for PLA + 5% hybrid. The fitting method was the same for the rest of the samples.

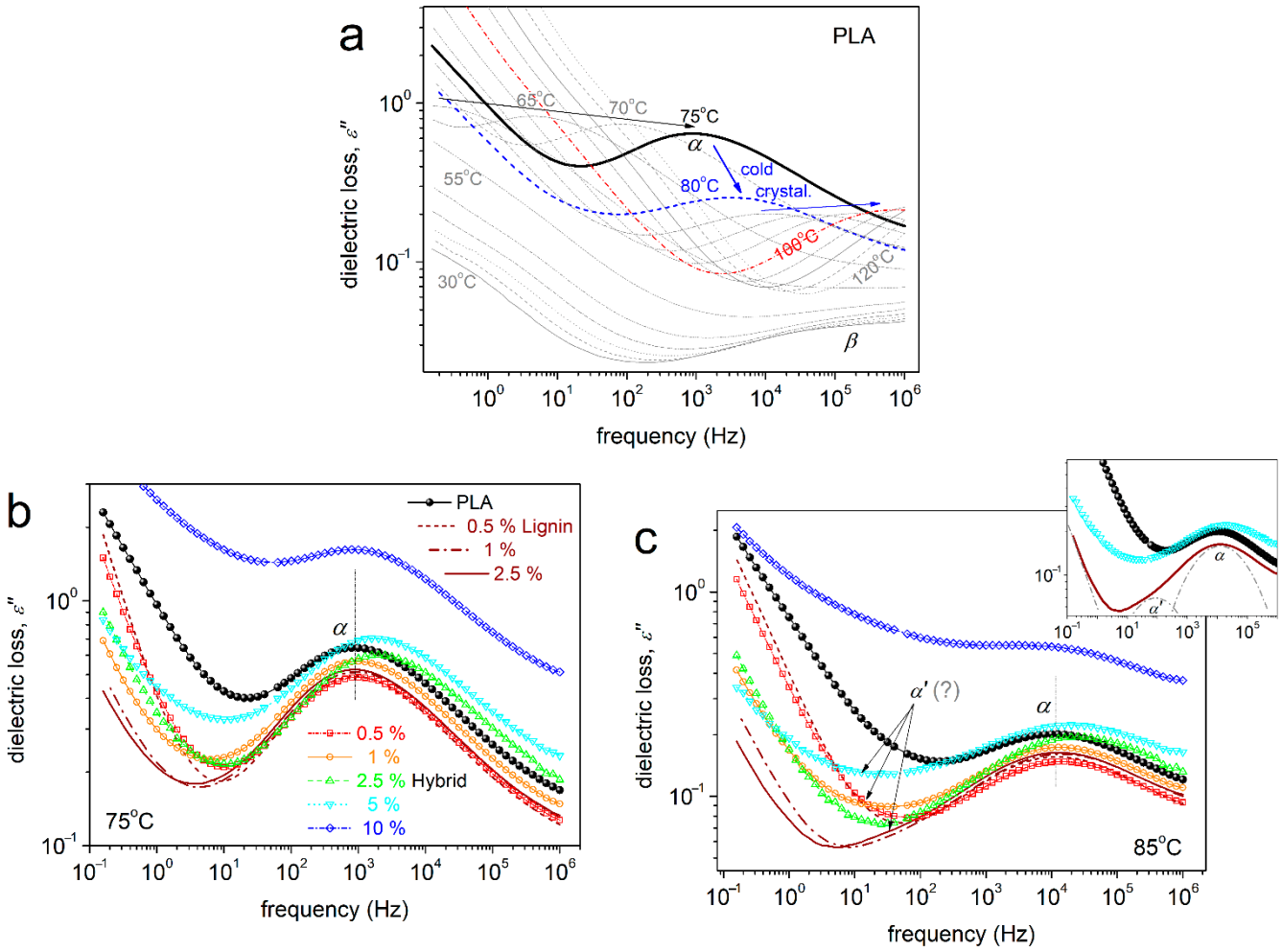


**Figure 10.** (**a**) Raw BDS data in the form of frequency and temperature dependence of the imaginary part of dielectric permittivity for neat PLA. Comparative ε″(f) for all samples at (**b**) 75 °C and (**c**) 85 °C. Indicated at selected temperatures are the recorded relaxation mechanisms (β, α, α′) as peaks and (**a**) the evolution of cold crystallization during the measurement.

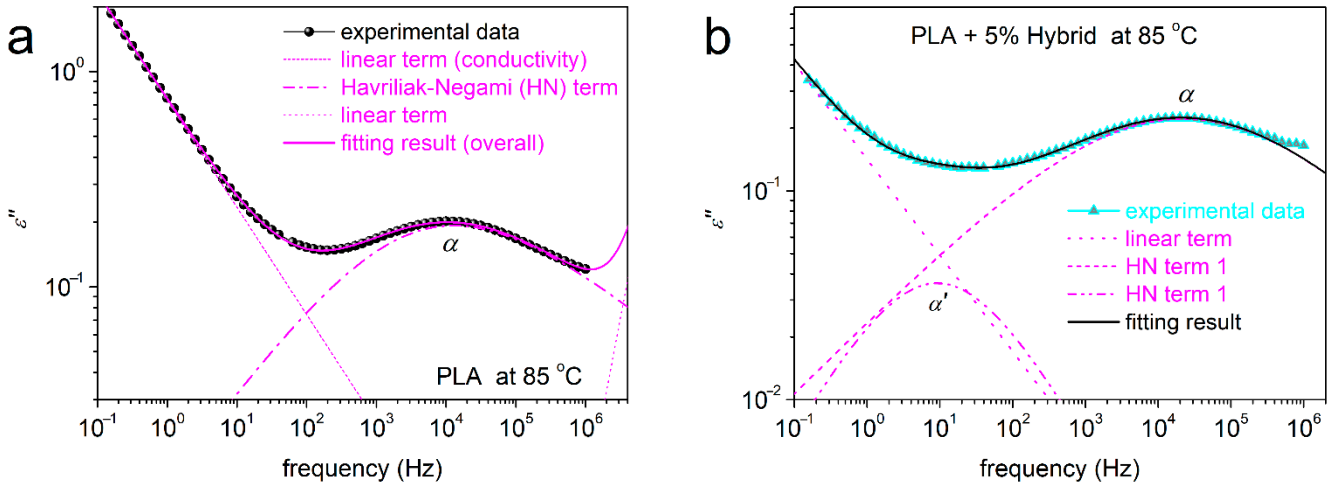


**Figure 11.** Examples of analysis of ε″(f) in terms of model functions, namely, selected for (**a**) neat PLA and (**b**) PLA + 5 wt% hybrid, at 85 °C.

Interestingly, the critical fitting was quite fruitful in the sense that for all PLA/hybrid and PLA + 1 and 2.5% lignin composites, an additional relaxation could be resolved. This

process, named as $\alpha'$ (e.g., in Figures 10b and 11b), was necessary to sufficiently fit the overall complex spectra. Actually, this an example of the power of analysis in BDS as an additional investigation tool [68,69,73,82]. In all cases and compared to $\alpha$, the $\alpha'$ relaxation was recorded at lower frequencies. This suggests slower/retarded mobility. In addition, $\alpha'$ relaxation exhibits significantly lower strength (magnitude). From the models/shape point of view, $\alpha$ could be fitted only with the asymmetric HN function ($\alpha_{HN}$~0.5–0.6, $\beta_{HN}$~0.6), whereas $\alpha'$ was fitted by the symmetric Cole–Cole function ($\alpha_{HN}$~0.6, $\beta_{HN}$~1).

From the fitting results, we were able to construct the so-called molecular dynamics map in terms of the reciprocal temperature, 1000/T, and dependence of the relaxation frequency maxima, $f_{max}$, for all relaxations. This is presented in Figure 12a, wherein, along with the dielectric data, we have added, for comparison, the calorimetric points for the glass transition temperature. In Figure 12b, we present the 1000/T dependence of $\Delta\varepsilon$, at the same temperature range.

In Figure 12b, $\alpha$ relaxation in neat PLA exhibits a 'curved' time scale, which is in accordance with previous studies on PLA [21,80,81] (and references therein). The curved time scale is characteristic for bulk cooperative dynamics. The trend can be mathematically expressed by the so-called Vogel–Fulcher–Tammann–Hesse (VFTH) equation (Equation (4)) [59,83].

$$f(T) = f_{0,VFTH} \cdot e^{-\frac{DT_0}{T-T_0}} \quad (4)$$

In Equation (3), $f_{0,VFTH}$ is a frequency constant and $T_0$ is the Vogel temperature at which $f_{0,VFTH} \to 0$. $D$ is the so-called fragility strength parameter [83]. The VFTH model was well fitted to our results on $\alpha$ and on $\alpha'$. In particular, for $\alpha$, the VFTH fitting was successful by fixing $f_{0,VFTH}$ to the phonon frequency of $10^{13}$ Hz [83], whereas this was not valid for $\alpha'$.

The time scale of $\alpha$ for PLA seems to not significantly change in the composites. However, we may observe a weak tendency for the acceleration of $\alpha$ for the larger loadings of hybrid. The result is quite similar to the effects recorded on the calorimetric $T_g$ (points in Figure 12a). The dielectric strength does not exhibit systematic alternations in the presence of the fillers, with the exception of PLA + 10% hybrid, wherein an overall significant $\Delta\varepsilon$ rise is recorded. This is, most probably, connected with the overall permittivity/conductivity rise for this sample, due to the presence of the highly conducting CNTs at a generally high amount (please compare with Figure 8b). Therefore, it is not essential to assign the increased $\Delta\varepsilon$ to stronger dipolar contribution (chain mobility).

From the time scale data on $\alpha$, we may estimate the $D$ parameter (Equation (4)) and, via the latter, calculate the fragility index for the segmental relaxation, $m_\alpha$. The calculation is performed employing Equation (5) [21,83].

$$m_\alpha = 16 + 590/D \quad (5)$$

Additionally, the dielectric glass transition temperature can be evaluated by extrapolating the VFTH fits to the equivalent frequency of conventional DSC at $T_g$, $f_{eq,DSC}$, i.e., when the chains' relaxation time becomes 100 s or else at $f_{eq,DSC}$~$10^{-2.8}$ Hz.

The $T_{g,diel}$ is shown comparatively with the calorimetric $T_g$, as a function of the filler loading in Figure 13a. The generally decreasing trends suggest that in the composites, there is a weak acceleration of the bulk-like polymer chains' diffusion. On the other hand, in Figure 13b, $m_\alpha$ (143 in PLA) exhibits a moderate increase in the composites (146–152), with the exception of the extreme case of PLA + 10% hybrid, where $m_\alpha$ is quite lower (138). The increased fragility, at least for simple polymer systems, can be discussed in terms of increased cooperativity levels and, equivalently, in terms of the shortening of the nanometric cooperativity length, $\xi$, [84,85]. We will come back to this point later.

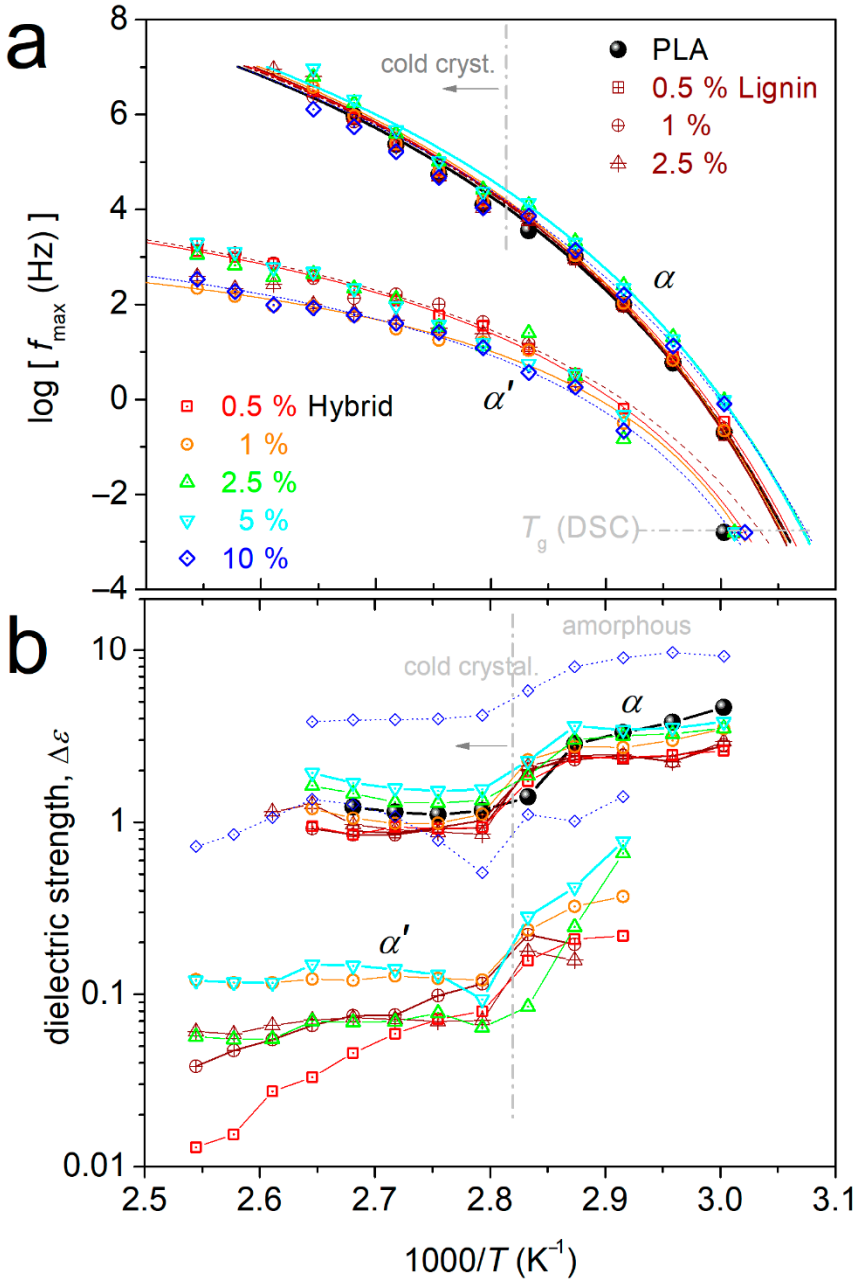


**Figure 12.** Dielectric relaxation map in terms of (**a**) Arrhenius diagrams for the time scale of all samples and relaxation and (**b**) the corresponding reciprocal temperature dependence of the dielectric strength. Added in (**a**) are the corresponding calorimetric values for $T_g$, while the added lines crossing the dielectric data are fittings of the Vogel–Tammann–Fulcher–Hesse equation on the points of α and α′ relaxation prior to the interference of cold crystallization.

We now come to the interesting case of α′ relaxation. The process exhibits a 'cooperative character', as manifested by the VFTH timescale in Figure 12a. Furthermore, upon its extrapolation to the calorimetric frequencies area in Figure 12a, the experimental data of α′ coincide quite well with the calorimetric $T_g$, similarly to the case of α relaxation. Combining these with the absence of the process in pure PLA, we may conclude that this is a segmental-like process with retarded (modified) dynamics arising from the interfacial polymer–filler region. Such a relaxation was observed for the first time in polydimethylsiloxane/silica nanocomposites by Fragiadakis et al. [68] and, later, within various other nanocomposites [66,69,70,73,82]. Adopting the methodologies used in these previous studies, we can estimate the amount of the interfacial polymer with the modified dynamics,

based on its dielectric strength ($\Delta\varepsilon_{\alpha}$ and $\Delta\varepsilon_{\alpha'}$, Figure 13b). We recall that in a previous section, we estimated the amount of the immobile interfacial polymer (RAF) based on its absent contribution to the calorimetric strength of the glass transition.

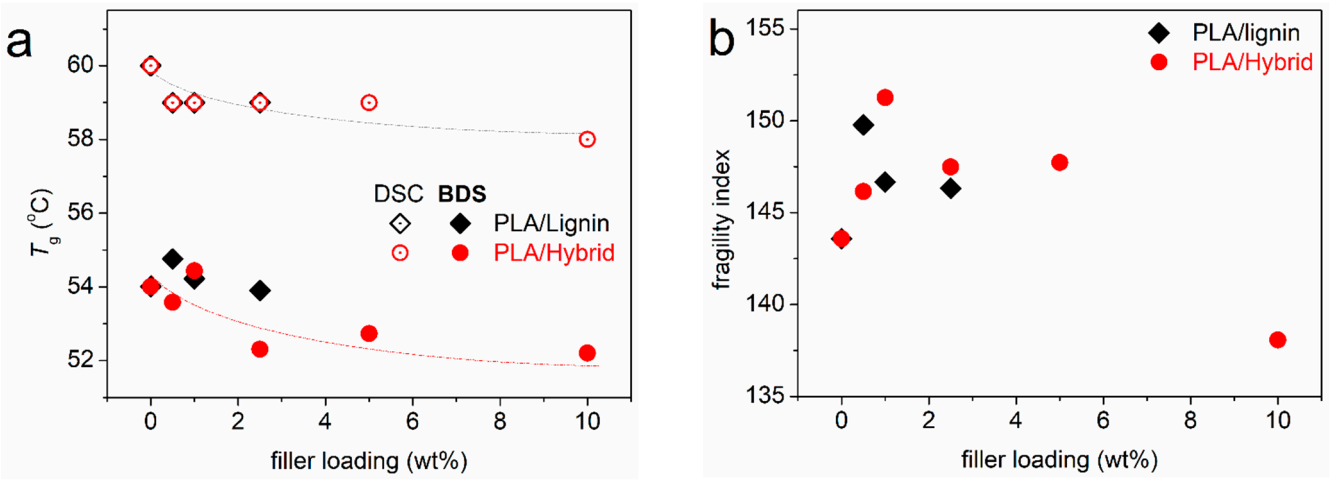


**Figure 13.** The filler content dependences of (**a**) the dielectric and calorimetric $T_g$s and (**b**) the fragility indices of α relaxation, for all systems. The added lines are used as guides for the eye.

Thus, employing some assumptions, for example, equal polarizability between the bulky and the interfacial chain' dipoles, we calculate the interfacial polymer fraction, IPF, by Equation (6) [66,69,70,73].

$$\mathrm{IPF} = \Delta\varepsilon_{\alpha'}/(\Delta\varepsilon_{\alpha} + \Delta\varepsilon_{\alpha'}) \quad (6)$$

The IPF values have been plotted against the filler loading and are shown comparatively with RAF (by DSC). The IPF values lay between 0% (PLA) and 10% (5% hybrid) and, for a fixed filler loading, they are significantly larger than those of the RAF (0–8%). Possibly, the RAF and IPF have different physical origins or/and the IPF may include the RAF (inset scheme in Figure 14) [66]. This is actually still an open debate in the literature. The filler loading dependence of RAF increases monotonically, whereas that of IPF does not, as it sharply increases even for the lowest hybrid amounts and barely increases further. This is possibly related to the parallel drop in the quality of the hybrid particles dispersion [73].

It should be reported that the shape parameters for α and α' relaxations ($\alpha_{HN}$ and $\beta_{HN}$) do not demonstrate any systematic or interesting changes between the different systems. Within previous cases, the values of '$\alpha_{HN} \times \beta_{HN}$' have been used as representatives of the relaxation times width [86], in other words, the degree of homogeneity of the relaxation modes.

We come back to the recorded discrepancy between DSC and BDS regarding the $T_g$ values (Figure 13a). Such or similar discrepancies have been recorded in the past within a variety of systems, especially when 'complex' polymeric phases are involved [57,87,88]. Next to the in-principle different techniques, a possible reason for the discrepancy has been proposed to originate from the existence of dynamical heterogeneities. Such heterogeneities are, for example, due to significant alternations in the cooperativity lengths, in particular, at different temperatures [89], being followed via different physical process (e.g., static and pure thermally in DSC, dielectrically and dynamically in BDS). Comparing with various nanocomposites studied by similar methods, Koutsoumpis et al. [88] concluded that the presence of an interfacial polymer may itself induce the said dynamical heterogeneities. This could be also the explanation in the present work.

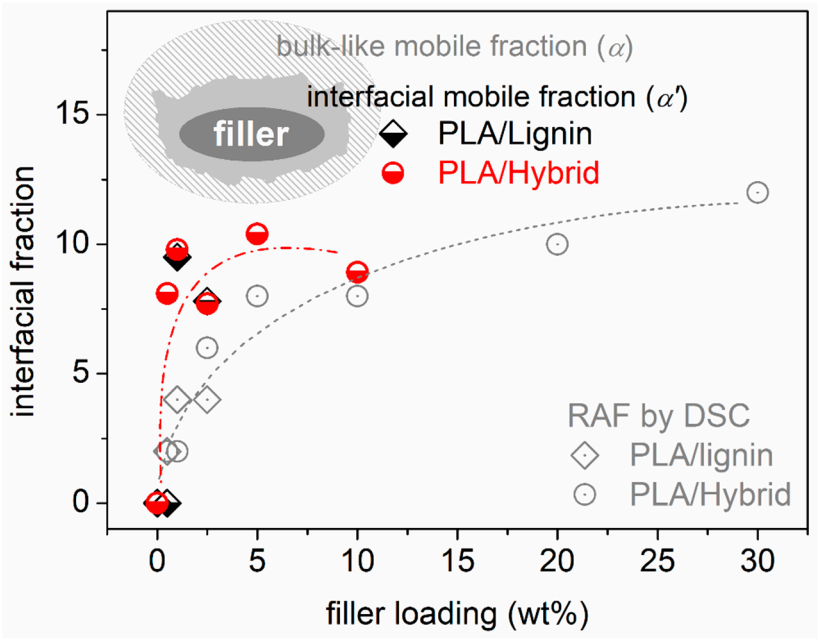


**Figure 14.** The interfacial polymer fraction as estimated from the dielectric and calorimetric data on segmental dynamics, being presented as a function of the filler wt% loading.

Finally, combining all the information together, we may conclude with a unified model for rationalizing the overall situation. An amount of PLA chains is concentrated around the hybrid particles, exhibiting a modified mobility (retarded or vanished). On the other hand, it seems that away from the particles, the bulky polymer may exhibit a slightly lesser density that enhances the PLA chain diffusion/mobility. Similar results rationalized by such scenarios have been recently reported for polyester-based complex systems (including PLA) [22,24,57].

## 4. Conclusions

For the recently synthesized PLA/hybrid (lignin–CNT), envisaged for use in conducting printing inks, a series of new results by complementary methods were recorded. The main results gained by the extensive investigation on the structure–properties relationships are as follows:

- PLA and lignin are electrical insulators due to the absence of free electrons. The conducting character (DC conductivity plateau) of the composites was offered by the addition of >2% CNTs. Interestingly, this was found true only in the case of hybrid particles, and not by the addition of neat CNTs in PLA at similar amounts.
- The result suggests an additional effect of lignin in the sense of facilitating the formation of CNT continuous paths (electronic percolation), which is, interestingly, compatible with the recorded microscopic view by SEM.
- For the composites, we obtained proofs for the formation of an interfacial polymer layer around the particles, without the implementation of strong polymer–particles interactions.
- A mild drop in the $T_g$ of PLA (60 °C), by 1–2 K, was recorded in the presence of the fillers, suggesting the formation of, in general, softer composites, compared with neat PLA.
- The latter is accompanied by the almost unchanged $T_m$ of PLA, which remains relatively low (174–176 °C).

These effects imposed by the hybrid particles are actually wanted, considering, on one hand, the envisaged application in printing inks (conductivity) and, on the other hand,

the processing in general. For example, we expect that the viscosity of the composites is lower than that of the unfilled PLA matrix. Among other indicators, this suggests a more beneficial processing with less energy consumption for the preparation and the application.

**Author Contributions:** Conceptualization, methodology, investigation, formal analysis, writing—original draft, P.A.K.; investigation, formal analysis, validation, writing—review and editing., R.O.I.; investigation, writing—review and editing, A.P.; investigation, formal analysis, writing—review and editing, S.P.M. and S.K.; investigation, validation, writing—review and editing, A.G.; resources, validation, writing—review and editing, I.D.; resources, supervision, validation, writing—review and editing, A.Z.-K.; investigation, formal analysis, validation, writing—review and editing, N.D.B.; resources, supervision, validation, writing—review and editing, A.K.; supervision, conceptualization, resources, validation, writing—review and editing, D.N.B. All authors have read and agreed to the published version of the manuscript.

**Funding:** This research was funded by the European Union under the GA no 101070556 (Sustain-a-Print, https://www.sustainaprint.eu/). Views and opinions expressed are however those of the author(s) only and do not necessarily reflect those of the European Union or RIA. Neither the European Union nor the granting authority can be held responsible for them.

**Data Availability Statement:** The DSC, FTIR, BDS and conductivity raw data are available on Zenodo (doi: https://doi.org/10.5281/zenodo.15281532). The rest of the data supporting this article will be available upon request to the corresponding authors, uniquely in the frame of private communication.

**Acknowledgments:** R.O. Ioannidis would like to thank Maria Nikopoulou and Eleni Pavlidou, from the Physics department of the Aristotle University of Thessaloniki (AUTH), Greece, for the SEM observations. P.A.K. would like to acknowledge Daniel Fragiadakis from the Naval Research Laboratory, Polymer Physics Section, Washington DC, USA for kindly providing his '*grafity*' data analysis software (http://grafitylabs.com/), which we have employed for analyzing the BDS data.

**Conflicts of Interest:** All authors declare that the research was conducted in the absence of any commercial or financial relationships that could be construed as a potential conflict of interest.

## References

1. Armentano, I.; Bitinis, N.; Fortunati, E.; Mattioli, S.; Rescignano, N.; Verdejo, R.; Lopez-Manchado, M.A.; Kenny, J.M. Multifunctional nanostructured PLA materials for packaging and tissue engineering. *Prog. Polym. Sci.* **2013**, *38*, 1720–1747. [CrossRef]
2. Auras, R.; Harte, B.; Selke, S. An overview of polylactides as packaging materials. *Macrom. Biosci.* **2004**, *4*, 835–864. [CrossRef]
3. Naser, A.Z.; Deiab, I.; Darras, B.M. Poly(lactic acid) (PLA) and polyhydroxyalkanoates (PHAs), green alternatives to petroleum-based plastics: A review. *RSC Adv.* **2021**, *11*, 17151–17196. [CrossRef]
4. Chanda, M.; Roy, S.K. *Industrial Polymers, Specialty Polymers, and Their Applications*; CRC Press: Boca Raton, FL, USA, 2008.
5. Rowan, S.J. 100th Anniversary of macromolecular science viewpoints. *ACS Macro Lett.* **2021**, *10*, 466–468. [CrossRef] [PubMed]
6. Sheldon, R.A.; Norton, M. Green chemistry and the plastic pollution challenge: Towards a circular economy. *Green Chem.* **2020**, *22*, 6310–6322. [CrossRef]
7. Oladapo, B.I.; Olawumi, M.A.; Olugbade, T.O.; Tin, T.T. Advancing sustainable materials in a circular economy for decarbonisation. *J. Environ. Manag.* **2024**, *360*, 121116. [CrossRef] [PubMed]
8. Garlotta, D. A literature review of poly(lactic acid). *J. Polym. Environ.* **2001**, *9*, 63–84. [CrossRef]
9. Saini, P.; Arora, M.; Kumar, M.N.V.R. Poly(lactic acid) blends in biomedical applications. *Adv. Drug Deliv. Rev.* **2016**, *107*, 47–59. [CrossRef]
10. Balla, E.; Daniilidis, V.; Karlioti, G.; Kalamas, T.; Stefanidou, M.; Bikiaris, N.D.; Vlachopoulos, A.; Koumentakou, I.; Bikiaris, D.N. Poly(lactic acid) a versatile biobased polymer of next decades with multifunctional properties. From monomer synthesis, polymerization techniques and molecular weight increase to PLA applications. *Polymers* **2021**, *13*, 1822. [CrossRef]
11. Ahmed, J.; Varshney, S.K. Polylactides-chemistry, properties and green packaging technology: A review. *Int. J. Food. Prop.* **2011**, *14*, 37–58. [CrossRef]
12. Lafraya, A.; Prieto, C.; Pardo-Figuerez, M.; Chiva, A.; Lagaron, J.M. Super-repellent paper coated with electrospun biopolymers and electrosprayed silica of interest in food packaging applications. *Nanomaterials* **2021**, *11*, 3354. [CrossRef] [PubMed]
13. Ngo, T.D.; Kashani, A.; Imbalzano, G.; Nquyen, K.T.Q.; Hui, D. Additive manufacturing (3D printing): A review of materials, methods, applications and challenges. *Compos. Part B Eng.* **2018**, *143*, 172–196. [CrossRef]

14. Constanzo, A.; Spotorno, R.; Candal, M.V.; Fernández, M.M.; Müller, A.J.; Graham, R.S.; Cavallo, D.; McIlroy, C. Residual alignment and its effect on weld strength in material-extrusion 3D-printing of polylactic acid. *Addit. Manuf.* **2020**, *36*, 101415.
15. Dominguez-Robles, J.; Martin, N.K.; Fong, M.L.; Stewart, S.A.; Irwin, N.J.; Rial-Hermida, M.I.; Donnelly, R.F.; Larrañeta, E. Antioxidant PLA composites containing lignin for 3D printing applications: A potential material for healthcare applications. *Pharmaceutics* **2019**, *11*, 165. [CrossRef]
16. Wang, B.; Wen, T.; Zhang, X.; Tercjak, A.; Dong, X.; Müller, A.J.; Wang, D.; Cavallo, D. Nucleation of poly(lactide) on the surface of different fibers. *Macromolecules* **2019**, *52*, 6274–6284. [CrossRef]
17. Casalini, T.; Rossi, F.; Castrovinci, A.; Perale, G. A perspective on polylactic acid-based polymers use for nanoparticles synthesis and applications. *Front. Bioeng. Biotechnol.* **2019**, *7*, 259. [CrossRef] [PubMed]
18. Sha, L.; Chen, Z.; Chen, Z.; Zhang, A.; Yang, Z. Polylactic acid based nanocomposites: Promising safe and biodegradable materials in biomedical field. *Int. J. Polym. Sci.* **2016**, *2016*, 6869154. [CrossRef]
19. Saeidlou, S.; Huneault, M.A.; Li, H.; Park, C.B. Poly(lactic acid) crystallization. *Prog. Polym. Sci.* **2012**, *37*, 1657–1667. [CrossRef]
20. Zhang, R.; Du, F.; Jariyavidyanont, K.; Zhuravlev, E.; Schick, C.; Androsch, R. Glass transition temperature of poly(d,l-lactic acid) of different molar mass. *Thermochim. Acta* **2022**, *718*, 179387. [CrossRef]
21. Klonos, P.A.; Bikiaris, N.D.; Barmpalexis, P.; Kyritsis, A. Segmental mobility in linear polylactides of various molecular weights. *Polymer* **2024**, *305*, 127177. [CrossRef]
22. Klonos, P.A.; Chronaki, K.; Vouyiouka, S.; Kyritsis, A. Effects of high crystallinity on the molecular mobility in poly(lactic acid)-based microcapsules. *ACS Appl. Polym. Mat.* **2024**, *6*, 1573–1583. [CrossRef]
23. Zhou, T.; Guo, Y.T.; Yang, C.; Meng, X.B.; Du, F.S.; Li, Z.C. High-Tg PLA copolymers via base-catalyzed transesterification of PLA with 2,5,7-trioxabicyclo[2.2.2]octan-6-one. *Polymer Chem.* **2024**, *15*, 156–165. [CrossRef]
24. Klonos, P.A.; Bikiaris, N.D.; Zamboulis, A.; Valera, M.A.; Mangas, A.; Kyritsis, A.; Terzopoulou, Z. Segmental mobility in sustainable copolymers based on poly(lactic acid) blocks built onto poly(butylene succinate) in situ. *Soft Matter* **2023**, *19*, 7846–7858. [CrossRef] [PubMed]
25. Androsch, R.; Zhang, R.; Schick, C. Melt-recrystallization of poly (l-lactic acid) initially containing $\alpha'$-crystals. *Polymer* **2019**, *176*, 227–235. [CrossRef]
26. Toda, A.; Androsch, R.; Schick, C. Insights into polymer crystallization and melting from fast chip calorimetry. *Polymer* **2016**, *91*, 239–263. [CrossRef]
27. Rahmanifard, M.; Khademi, S.M.H.; Asheghi-Oskooee, R.; Farizeh, T.; Hemmati, F. Reactive processing-microstructure-mechanical performance correlations in biodegradable poly(lactic acid)/expanded graphite nanocomposites. *RSC Adv.* **2024**, *14*, 794–807. [CrossRef]
28. Klonos, P.; Terzopoulou, Z.; Koutsoumpis, S.; Zidropoulos, S.; Kripotou, S.; Papageorgiou, G.Z.; Bikiaris, D.; Kyritsis, A.; Pissis, P. Rigid amorphous fraction and segmental dynamics in nanocomposites based on poly(L-lactic acid) and nano-inclusions of 1-3D geometry studied by thermal and dielectric techniques. *Eur. Polym. J.* **2016**, *82*, 16–34. [CrossRef]
29. Georgiopoulos, P.; Kontou, E.; Meristoudi, A.; Pispas, S.; Chatzinikolaidou, M. The effect of silica nanoparticles on the thermomechanical properties and degradation behavior of polylactic acid. *J. Biomat. Appl.* **2014**, *29*, 662–674. [CrossRef]
30. Lin, J.; Shenogin, S.; Nazarenko, S. Oxygen solubility and specific volume of rigid amorphous fraction in semicrystalline poly(ethylene terephthalate). *Polymer* **2002**, *43*, 4733–4743. [CrossRef]
31. Safandowska, M.; Makarewicz, C.; Rozanski, A.; Idczak, R. Barrier properties of semicrystalline polylactide: The role of the density of the amorphous regions. *Macromolecules* **2022**, *55*, 10077–10089. [CrossRef]
32. Klonos, P.A.; Peoglos, V.; Bikiaris, D.N.; Kyritsis, A. Rigid amorphous fraction and thermal diffusivity in nanocomposites based on poly(L-lactic acid) filled with carbon nanotubes and graphene oxide. *J. Phys. Chem. C* **2020**, *123*, 5469–5479. [CrossRef]
33. Klonos, P.A.; Bikiaris, R.D.; Terzopoulou, Z.; Mouchlianiti, K.; Tsachouridis, K.; Anastasiou, A.D.; Kyritsis, A.; Kyzas, G.Z. Structure-properties relationships in new polymer nanocomposites based on the renewable poly(butylene succinate) filled with low amounts of nanoparticles of 1-3D geometries. *Polymer* **2024**, *296*, 126841. [CrossRef]
34. Ainali, N.M.; Kalaronis, D.; Evgenidou, E.; Kyzas, G.Z.; Bobori, D.C.; Kaloyianni, M.; Yang, X.; Bikiaris, D.N.; Lambropoulou, D.A. Do poly(lactic acid) microplastics instigate a threat? A perception for their dynamic towards environmental pollution and toxicity. *Sci. Tot. Environ.* **2022**, *832*, 155014. [CrossRef]
35. Naddeo, M.; Viscusi, G.; Gorrasi, G.; Pappalardo, D. Degradable elastomers: Is there a future in tyre compound formulation? *Molecules* **2021**, *26*, 4454. [CrossRef]
36. Stauffer, D.; Aharony, A. *Introduction to Percolation Theory*; Taylor and Francis: London, UK, 1985.
37. Logakis, E.; Pollatos, E.; Pandis, C.; Peoglos, V.; Zuburtikudis, I.; Delidis, C.G.; Vatalis, A.; Gjoka, M.; Syskakis, E.; Viras, K. Structure-property relationships in isotactic polypropylene/multi-walled carbon nanotubes nanocomposites. *Compos. Sci. Technol.* **2010**, *70*, 328–335. [CrossRef]
38. Sandler, J.K.W.; Kirk, J.E.; Kinloch, I.A.; Shaffer, M.S.P.; Windle, A.H. Ultra-low electrical percolation threshold in carbon-nanotube-epoxy composites. *Polymer* **2003**, *44*, 5893–5899. [CrossRef]

39. Sam-Daliri, O.; Faller, L.M.; Farahani, M.; Roshanghias, A.; Araee, A.; Baniassadi, M.; Oberlercher, H.; Zangl, H. Impedance analysis for condition monitoring of single lap CNT-epoxy adhesive joint. *Int. J. Adhes. Adhes.* **2019**, *88*, 59–65. [CrossRef]
40. Zhang, H.; Bilotti, E.; Peijs, T. The use of carbon nanotubes for damage sensing and structural health monitoring in laminated composites: A review. *Nanocomposites* **2015**, *1*, 167–184. [CrossRef]
41. Sam-Daliri, O.; Faller, L.M.; Farahani, M.; Zangl, H. Structural health monitoring of adhesive joints under pure mode I loading using the electrical impedance measurement. *Eng. Fract. Mech.* **2021**, *245*, 107585. [CrossRef]
42. Bie, Z.; Liu, X.; Deng, Y.; Shi, X.; He, X. Study on crack resistance mechanism of helical carbon nanotubes in nanocomposites. *Nanomaterials* **2025**, *15*, 119. [CrossRef]
43. Meegan, J. Some of the challenges faced by the Composites Industry in its bid to become more sustainable. *RSC Sustain.* **2023**, *1*, 1737–1742. [CrossRef]
44. Terzopoulou, Z.; Bikiaris, D.N. Biobased plastics for the transition to a circular economy. *Mater. Lett.* **2024**, *362*, 136174. [CrossRef]
45. Sternberg, J.; Sequerth, O.; Pilla, S. Green chemistry design in polymers derived from lignin: Review and perspective. *Prog. Polym. Sci.* **2021**, *113*, 101344. [CrossRef]
46. Mohanty, A.K.; Wu, F.; Micheva, R.; Hakkarainen, M.; Raquez, J.-M.; Mielewski, D.H.; Narayan, R.; Netravali, A.N.; Misra, M. Sustainable polymers. *Nat. Rev. Methods Primers* **2022**, *2*, 46. [CrossRef]
47. Ma, C.; Kim, T.H.; Liu, K.; Ma, M.G.; Choi, S.E.; Si, C. Multifunctional lignin-based composite materials for emerging applications. *Front. Bioeng. Biotechnol.* **2021**, *9*, 708976. [CrossRef]
48. Gordobil, O.; Delucis, R.; Egüés, I.; Labidi, J. Kraft lignin as filler in PLA to improve ductility and thermal properties. *Ind. Crops Prod.* **2015**, *72*, 46–53. [CrossRef]
49. Zhang, Y.; Naebe, M. Lignin: A review on structure, properties, and applications as a light-colored UV absorber. *ACS Sustain. Chem. Eng.* **2021**, *9*, 1427–1442. [CrossRef]
50. Li, J.; Liu, W.; Qiu, X.; Zhao, X.; Chen, Z.; Yan, M.; Fang, Z.; Li, Z.; Tu, Z.; Huang, J. Lignin: A sustainable photothermal block for smart elastomers. *Green Chem.* **2022**, *24*, 823–836. [CrossRef]
51. Domínguez-Robles, J.; Larrañeta, E.; Fong, M.L.; Martin, N.K.; Irwin, N.J.; Mutjé, P.; Tarrés, Q.; Delgado-Aguilar, M. Lignin/poly(butylene succinate) composites with antioxidant and antibacterial properties for potential biomedical applications. *Int. J. Biol. Macrom.* **2020**, *145*, 92–99. [CrossRef]
52. Ullah, I.; Chen, Z.; Xie, Y.; Khan, S.S.; Singh, S.; Yu, C.; Cheng, G. Recent advances in biological activities of lignin and emerging biomedical applications: A short review. *Int. J. Biol. Macrom.* **2022**, *208*, 819–832. [CrossRef]
53. Domenek, S.; Louaifi, A.; Guinault, A.; Baumberger, S. Potential of lignins as antioxidant additive in active biodegradable packaging materials. *J. Polym. Environ.* **2013**, *21*, 692–701. [CrossRef]
54. Makri, S.P.; Xanthopoulou, E.; Valera, M.Á.; Mangas, A.; Marra, G.; Ruiz, V.; Koltsakidis, S.; Tzetzis, D.; Zoikis Karathanasis, A.; Deligkiozi, I.; et al. Poly(lactic acid) composites with lignin and nanolignin synthesized by in situ reactive processing. *Polymers* **2023**, *15*, 2386. [CrossRef] [PubMed]
55. Shi, K.; Liu, G.; Sun, H.; Weng, Y. Polylactic acid/lignin composites: A review. *Polymers* **2023**, *15*, 2807. [CrossRef] [PubMed]
56. Gordobil, O.; Eques, I.; Llano-Ponte, R.; Labidi, J. Physicochemical properties of PLA lignin blends. *Polym. Degrad. Stab.* **2014**, *108*, 330–338. [CrossRef]
57. Makri, S.P.; Klonos, P.A.; Marra, G.; Zoikis Karathanasis, A.; Deligkiozi, I.; Valera, M.Á.; Mangas, A.; Nikolaidis, N.; Terzopoulou, Z.; Kyritsis, A.; et al. Structure–property relationships in renewable composites of poly(lactic acid) reinforced by low amounts of micro- and nano-kraft-lignin. *Soft Matter* **2024**, *20*, 5014–5027. [CrossRef]
58. Makri, S.; Grigoropoulos, A.; Bikiaris, D.; Geligkiozi, I.; Zoikis-Karathanasis, A. assignee Creative Nano P.C. Ultrasound-AsSisted Process for the Production of Lignin Nanoparticles, p. European Patent Office. EP4471093A1, 4 December 2024.
59. Kremer, F.; Schönhals, A. (Eds.) *Broadband Dielectric Spectroscopy*; Springer: New York, NY, USA, 2003. [CrossRef]
60. Leng, J.; Kang, N.; Wang, D.Y.; Wurm, A.; Schick, C.; Schönhals, A. Crystallization behavior of nanocomposites based on poly(l-lactide) and MgAl layered double hydroxides–Unbiased determination of the rigid amorphous phases due to the crystals and the nanofiller. *Polymer* **2017**, *108*, 257–264. [CrossRef]
61. Righetti, M.C.; Gazzano, M.; Delpouve, N.; Saiter, A. Contribution of the rigid amorphous fraction to physical ageing of semi-crystalline PLLA. *Polymer* **2017**, *125*, 241–253. [CrossRef]
62. De Bortoli, L.S.; de Farias, R.; Mezalira, D.Z.; Schabbach, L.M.; Fredel, M.C. Functionalized carbon nanotubes for 3D-printed PLA-nanocomposites: Effects on thermal and mechanical properties. *Mat. Tod. Commun.* **2022**, *31*, 103402. [CrossRef]
63. Lage-Rivera, S.; Ares-Pernas, A.; Becerra Permuy, J.C.; Gosset, A.; Abad, M.J. Enhancement of 3D printability by FDM and electrical conductivity of PLA/MWCNT filaments using lignin as bio-dispersant. *Polymers* **2023**, *15*, 999. [CrossRef]
64. Sargsyan, A.; Tonoyan, A.; Davtyan, S.; Schick, C. The amount of immobilized polymer in PMMA $SiO_2$ nanocomposites determined from calorimetric data. *Eur. Polym. J.* **2007**, *43*, 3113–3127. [CrossRef]
65. Wurm, A.; Ismail, M.; Kretzschmar, B.; Pospiech, D.; Schick, C. Retarded crystallization in polyamide/layered silicates nanocomposites caused by an immobilized interphase. *Macromolecules* **2010**, *43*, 1480–1487. [CrossRef]

66. Klonos, P.; Kulyk, K.; Borysenko, M.V.; Gun'ko, V.M.; Kyritsis, A.; Pissis, P. Effects of molecular weight below the entanglement threshold on interfacial nanoparticles/polymer dynamics. *Macromolecules* **2016**, *49*, 9457–9473. [CrossRef]
67. Leng, J.; Szymoniak, P.; Kang, N.J.; Wang, D.Y.; Wurm, A.; Schick, C.; Schönhals, A. Influence of interfaces on the crystallization behavior and the rigid amorphous phase of poly(L-lactide)-based nanocomposites with different layered double hydroxides as nanofiller. *Polymer* **2019**, *184*, 121929. [CrossRef]
68. Fragiadakis, D.; Pissis, P.; Bokobza, L. Glass transition and molecular dynamics in poly(dimethylsiloxane)/silica nanocomposites. *Polymer* **2005**, *46*, 6001–6008. [CrossRef]
69. Füllbrandt, M.; Purohit, P.J.; Schönhals, A. Combined FTIR and dielectric investigation of poly(vinyl acetate) adsorbed on silica particles. *Macromolecules* **2013**, *46*, 4626–4632. [CrossRef]
70. Holt, A.P.; Griffin, P.J.; Bocharova, V.; Agapov, A.L.; Imel, A.E.; Dadmun, M.D.; Sangoro, J.R.; Sokolov, A.P. Dynamics at the polymer/nanoparticle interface in poly(2-vinylpyridine)/silica nanocomposites. *Macromolecules* **2014**, *47*, 1837–1843. [CrossRef]
71. Androsch, R.; Di Lorenzo, M.L.; Schick, C.; Wunderlich, B. Mesophases in polyethylene polypropylene, and poly(1-butene). *Polymer* **2010**, *51*, 4639–4662. [CrossRef]
72. Purohit, P.J.; Wang, D.Y.; Wurm, A.; Schick, C.; Schönhals, A. Comparison of thermal and dielectric spectroscopy for nanocomposites based on polypropylene and layered double hydroxide–proof of interfaces. *Eur. Polym. J.* **2014**, *55*, 48–56. [CrossRef]
73. Fragiadakis, D.; Bokobza, L.; Pissis, P. Dynamics near the filler surface in natural rubber-silica nanocomposites. *Polymer* **2011**, *52*, 3175–3182. [CrossRef]
74. Kim, Y.G.; Thérien-Aubin, H. Impact of the solvent quality on the local dynamics of soft and swollen polymer nanoparticles functionalized with polymer chains. *Macromolecules* **2020**, *53*, 7561–7569. [CrossRef]
75. Beigbeder, A.; Linares, M.; Devalckenaere, M.; Degée, P.; Claes, M.; Beljonne, D.; Lazzaroni, R.; Dubois, P. CH-π interactions as the driving force for silicone-based nanocomposites with exceptional properties. *Adv. Mater.* **2008**, *20*, 1003–1007. [CrossRef]
76. Tadiello, L.; D'Arienzo, M.; Di Credico, B.; Hanel, T.; Matejka, L.; Mauri, M.; Morazzoni, F.; Simonutti, R.; Spirkova, M.; Scotti, R. The filler–rubber interface in styrene butadiene nanocomposites with anisotropic silica particles: Morphology and dynamic properties. *Soft Matter* **2015**, *11*, 4022–4033. [CrossRef]
77. Fischer, E.W.; Sterzel, H.J.; Wegner, G. Investigation of the structure of solution grown crystals of lactide copolymers by means of chemical reactions. *Kolloid-Z. Z. Polym.* **1973**, *251*, 980–990. [CrossRef]
78. Logakis, E.; Pissis, P.; Pospiech, D.; Korwitz, A.; Krause, B.; Reuter, U.; Pötschke, P. Low electrical percolation threshold in poly(ethylene terephthalate)/multi-walled carbon nanotube nanocomposites. *Eur. Polym. J.* **2010**, *46*, 928–936. [CrossRef]
79. Qu, F.; Sun, W.; Li, B.; Li, F.; Gao, Y.; Zhao, X.; Zhang, L. Synergistic effect in improving the electrical conductivity in polymer nanocomposites by mixing spherical and rod-shaped fillers. *Soft Matter* **2020**, *16*, 10454–10462. [CrossRef] [PubMed]
80. Ren, J.; Urakawa, O.; Adachi, K. Dielectric study on dynamics and conformations of poly(D,L-lactic acid) in dilute and semi-dilute solutions. *Polymer* **2003**, *44*, 847–855. [CrossRef]
81. Brás, A.R.; Viciosa, M.T.; Wang, Y.; Dionisio, M.; Mano, J.F. Crystallization of poly(L–lactic acid) probed with dielectric relaxation spectroscopy. *Macromolecules* **2006**, *39*, 6513–6520. [CrossRef]
82. Lin, Y.; Liu, L.; Xu, G.; Zhang, D.; Guan, A.; Wu, G. Interfacial interactions and segmental dynamics of poly(vinyl acetate)/silica nanocomposites. *J. Phys. Chem. C* **2015**, *119*, 12956–12966. [CrossRef]
83. Böhmer, R.; Ngai, K.; Angell, C.A.; Plazek, D.J. Nonexponential relaxations in strong and fragile glass formers. *J. Chem. Phys.* **1993**, *99*, 4201–4209. [CrossRef]
84. Adam, G.; Gibbs, J.H. On the temperature dependence of cooperative relaxation properties in glass-forming liquids. *J. Chem. Phys.* **1965**, *43*, 139–146. [CrossRef]
85. Delpouve, N.; Saiter, A.; Dargent, E. Cooperativity length evolution during crystallization of poly(lactic acid). *Eur. Polym. J.* **2011**, *47*, 2414–2423. [CrossRef]
86. Schönhals, A.; Szymoniak, P. (Eds.) *Dynamics of Composite Materials*; Springer: Cham, Switzerland, 2022.
87. Madkour, S.; Yin, H.; Füllbrandt, M.; Schönhals, A. Calorimetric evidence for a mobile surface layer in ultrathin polymeric films: Poly(2-vinyl pyridine). *Soft Matter* **2015**, *11*, 7942–7958. [CrossRef] [PubMed]
88. Koutsoumpis, S.; Raftopoulos, K.N.; Oguz, O.; Papadakis, C.M.; Menceloglu, Y.Z.; Pissis, P. Dynamic glass transition of the rigid amorphous fraction in polyurethane-urea/SiO2 nanocomposites. *Soft Matter* **2017**, *13*, 4580–4590. [CrossRef] [PubMed]
89. Monnier, X.; Cangialosi, D. Thermodynamic ultrastability of a polymer glass confined at the micrometer length Scale. *Phys. Rev. Lett.* **2018**, *121*, 137801. [CrossRef]